

# Gas outflows in two recently quenched galaxies at $z = 4$ and 7

F. Valentino<sup>1,2,3</sup>, K. E. Heintz<sup>1,4,5</sup>, G. Brammer<sup>1,4</sup>, K. Ito<sup>1,2,6</sup>, V. Kokorev<sup>7</sup>, K. E. Whitaker<sup>8,1</sup>, A. Gallazzi<sup>9</sup>, A. de Graaff<sup>10</sup>, A. Weibel<sup>5</sup>, B. L. Frye<sup>11</sup>, P. S. Kamieneski<sup>12</sup>, S. Jin<sup>1,2</sup>, D. Ceverino<sup>13,14</sup>, A. Faisst<sup>15</sup>, M. Farcy<sup>16</sup>, S. Fujimoto<sup>7</sup>, S. Gillman<sup>1,2</sup>, R. Gottumukkala<sup>1,4</sup>, M. Hamadouche<sup>8</sup>, K. C. Harrington<sup>17,18,19,20</sup>, M. Hirschmann<sup>16</sup>, C. K. Jespersen<sup>21</sup>, T. Kakimoto<sup>22,23</sup>, M. Kubo<sup>24,25</sup>, C. d. P. Lagos<sup>26,1</sup>, M. Lee<sup>1,2</sup>, G. E. Magdis<sup>1,2</sup>, A. W. S. Man<sup>27</sup>, M. Onodera<sup>22,23,28</sup>, F. Rizzo<sup>29</sup>, R. Shimakawa<sup>30</sup>, D. J. Setton<sup>31</sup>, M. Tanaka<sup>22,23</sup>, S. Toft<sup>1,4</sup>, P.-F. Wu<sup>32</sup>, and P. Zhu<sup>1,2</sup>

(Affiliations can be found after the references)

Received –; accepted –

## ABSTRACT

Outflows are a key element in the baryon cycle of galaxies, impacting their evolution by extracting gas, momentum, and energy and then injecting them into the surrounding medium. The properties of gas outflows provide a fundamental test for our models of how galaxies transition from a phase of active star formation to quiescence. Here we report the detection of outflowing gas signatures in two recently quenched, massive ( $M_\star \sim 10^{10.2} M_\odot$ ) galaxies at  $z = 4.106$  (NS\_274) and  $z = 7.276$  (RUBIES-UDS-QG-z7) observed at rest-frame ultraviolet to near-infrared wavelengths with JWST/NIRSpec. The outflows are traced by blueshifted magnesium (MgII) absorption lines, and in the case of the  $z = 4.1$  system, also by iron (FeII) and sodium (NaI) features. Together, these transitions broadly trace the chemically enriched neutral phase of the gaseous medium. The rest-frame optical spectra of the two sources are similar to those of local post-starburst galaxies, showing deep Balmer stellar features, a relatively low  $D_n4000$  index, and minimal ongoing star formation on 10 Myr timescales, as traced by the lack of bright nebular and recombination emission lines. This also suggests the absence of strong and radiatively efficient active galactic nucleus activity. The galaxies' star formation histories are consistent with a recent and abrupt quenching, prior to which the average star formation rate was  $\sim 15 M_\odot \text{ yr}^{-1}$  over the last 100 Myr of their lives. In the case of NS\_274, dedicated millimeter observations allowed us to also strongly constrain the dust obscured star formation rate to  $< 12 M_\odot \text{ yr}^{-1}$ , unambiguously confirming its quiescence. Under simple geometrical assumptions, we derive mass loading factors  $\eta = \dot{M}_{\text{out}}/\text{SFR}_{100 \text{ Myr}} \lesssim 1$  and  $> 10$  for the  $z = 4.1$  and  $z = 7.3$  systems, respectively, and a similarly pronounced difference in the energy carried by the outflows. Supernova feedback could account for the mass and energy of the outflow in NS\_274. However, the low mass loading factor and average gas velocity ( $\sim 180 \text{ km s}^{-1}$ , which is lower than the stellar velocity dispersion) suggest that the observed outflow is likely not the primary factor behind the quenching of NS\_274, but it might represent a relic of the star formation process winding down. Star-formation-related processes seem to also be insufficient to explain the extreme mass outflow rate of RUBIES-UDS-QG-z7, which would require an additional ejective mechanism such as an undetected active galactic nucleus. Finally, the average outflow velocities per unit stellar mass, star formation rate, and surface density of star formation rate are consistent with those of lower-redshift post-starburst galaxies, suggesting that outflows in rapidly quenched galaxies might occur similarly across cosmic time. Our findings hint at the existence of a rich tapestry of galaxy quenching pathways at high redshifts, and they highlight the importance of using large spectroscopic samples that map different spectral features to account for the different timescales on which different mechanisms contribute to this process.

**Key words.** Galaxies: evolution, high-redshift, stellar content; ISM: jets and outflows.

## 1. Introduction

The physical mechanisms responsible for the suppression of star formation in galaxies remain a major topic of debate in modern astrophysics, especially after the spectroscopic confirmation of massive (stellar masses of  $M_\star \sim 10^{10-11} M_\odot$ ) “quenched” systems in the first few hundred million years ( $z \sim 3-7$ ) of our Universe's history (Glazebrook et al. 2017; Schreiber et al. 2018a; Tanaka et al. 2019; Valentino et al. 2020; Forrest et al. 2020a,b, 2022; Carnall et al. 2023, 2024; Nanayakkara et al. 2024; Glazebrook et al. 2024; Urbano Stawinski et al. 2024; Tanaka et al. 2024; Kakimoto et al. 2024; Setton et al. 2024; Onoue et al. 2024; Kokorev et al. 2024; Antwi-Danso et al. 2025; de Graaff et al. 2025b; Turner et al. 2025; Wu 2025; Weibel et al. 2025; Baker et al. 2025 among others). Models and simulations have to invoke powerful winds and gas ejection powered by active galactic nuclei (AGNs) in order to reproduce stellar masses and stellar mass functions at  $z = 0$ , with a lesser role played by star formation feedback, especially at the highest masses (see the reviews by Somerville & Davé 2015; Naab & Ostriker 2017). However, despite the huge effort to refine the feedback recipes

implemented in models, the number density and stellar masses of quenched galaxies at  $z > 3$  represent a challenge in most, if not all, state-of-the-art cosmological simulations (e.g., Schreiber et al. 2018a; Merlin et al. 2019; Valentino et al. 2020, 2023; De Lucia et al. 2024; Lagos et al. 2025; Xie et al. 2024; Baker et al. 2025).

The exact details of the physical models of AGN and stellar feedback differ from simulation to simulation, but outflows remain a staple mechanism to quench galaxies in most available models (Kurinchi-Vendhan et al. 2024; Lagos et al. 2025). Different recipes and implementations might result in equally robust stellar mass functions in the local Universe, but they predict different outflow properties – which thus become a powerful tool for gaining insight into the physics governing galaxies. Observationally, multiphase gas flowing outward from star-forming galaxies or systems harboring actively growing supermassive black holes is well documented, especially up to cosmic noon, based on the detection of both emission and absorption lines across the whole electromagnetic spectrum (e.g., Förster Schreiber & Wuyts 2020; Veilleux et al. 2020). Focusing on the

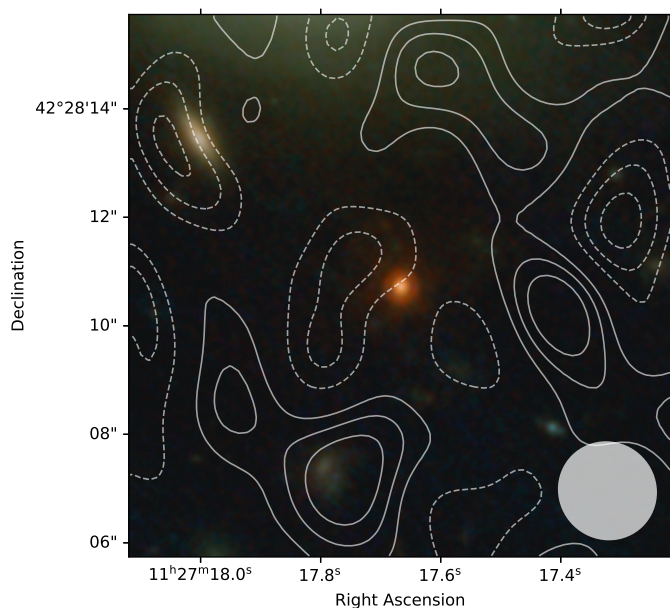


Fig. 1: RGB color image of NS\_274 at  $z = 4.1061$  overlaid with NOEMA 1.3 mm contours. The  $10'' \times 10''$  background image is a color composite of six available wide-band NIR-Cam filters. The dashed and solid white contours indicate the  $[-3\sigma, -2\sigma, -1\sigma, 1\sigma, 2\sigma, 3\sigma]$  dust continuum emission at a  $260 \mu\text{m}$  rest frame wavelength, determined with NOEMA observations. The elliptical patch indicates the size of the beam.

colder and denser outflow phases, the detection of low ionization absorption features in the rest-frame ultraviolet (UV) spectrum of galaxies has been a chief probe of their properties (e.g., Frye et al. 2002; Shapley et al. 2003; Rupke et al. 2005; Veilleux et al. 2005; Weiner et al. 2009; Rubin et al. 2014; Veilleux et al. 2020; Xu et al. 2022; Mingozi et al. 2022). This allowed the outflow properties to be mapped across a large dynamic range of host galaxy properties and various scaling relations to be established (e.g., the average and maximum outflow velocity vs. stellar mass, star formation rate, and surface densities; see Davis et al. 2023, and references therein).

In massive systems, the mixture of intense star formation and the simultaneous growth of central black holes makes the outflow phenomenon more complicated to decipher. Moreover, studying the population of recently quenched systems that likely experienced the effects of both supernova (SN) and AGN-powered feedback in their recent past, and are on their way to quiescence, has been a particularly difficult task to undertake given their relative rarity after cosmic noon and faintness at UV wavelengths. In general, most observational studies ascertained the presence of outflowing gas in recently quenched systems, both in the presence and absence of ongoing AGN activity (e.g., Tremonti et al. 2007; Coil et al. 2011; Maltby et al. 2019; Baron et al. 2020, 2022; Man et al. 2021; Davis et al. 2023; Taylor et al. 2024; Sun et al. 2024).

At higher redshifts, when approaching the main epoch of quenching of the most massive systems, galaxies showing typical “post-starburst” signatures, such as deep Balmer absorption lines, shallow  $D_n4000$  breaks, and weak emission lines, naturally become more common (D’Eugenio et al. 2020; Forrest et al. 2020b). This makes the study of this population more appealing and urgent – and, thanks to JWST, feasible. Interestingly, AGNs seem to be common in recently quenched

galaxies at  $z = 2 - 3$  and above. Extreme optical line ratios, broad emission features, and mid-infrared detections are routinely reported (e.g., Carnall et al. 2023; D’Eugenio et al. 2024; Belli et al. 2024; Nanayakkara et al. 2024; Kokorev et al. 2024; Onoue et al. 2024; Ji et al. 2024). Ionized outflows on their own (e.g., Kubo et al. 2022) are likely not sufficient to quench star formation, but signatures of massive amounts of neutral gas leaving quenched galaxies at  $z = 2 - 3$  have recently been reported in the literature (D’Eugenio et al. 2024; Belli et al. 2024; Davies et al. 2024). The simultaneous presence of high-velocity ( $\sim 1000 \text{ km s}^{-1}$ ) neutral outflows and AGN signatures has been interpreted as the smoking gun of a causal connection between the activity of supermassive black holes and quenching. However, the contribution to the mass and energy budget of cold outflows due to the last episode of star formation or its residuals is yet to be fully understood (see, e.g., Rupke et al. 2019, for an example of a starburst-driven outflow in a massive galaxy). This is especially true in the presence of outflows less extreme in terms of velocity and mass.

In this work we studied two distant and recently quenched galaxies that show signatures of outflowing gas: NS\_274 at  $z = 4.106$  and RUBIES-UDS-QG-z7 at  $z = 7.276$ . Their redshifts were first confirmed with JWST/NIRSpec observations in Frye et al. (2024) and Weibel et al. (2025), respectively. These two sources stand out as the most distant quenched galaxies with high S/N coverage of the rest-frame UV and optical spectra at medium and high spectral resolution in our archival search and dedicated survey with JWST/NIRSpec (the “DeepDive” project; Ito et al. in prep.). They thus allowed us to explore a new redshift regime; future work on population studies at lower redshifts ( $z \sim 2 - 3$ ) will follow. In particular, in this work we confirm and refine the redshift of RUBIES-UDS-QG-z7 thanks to newly acquired data with a G235M/F170LP grating and filter combination, and a custom reduction pipeline that is able to recover the whole wavelength coverage allowed by the long-pass filter and position on the detector (Brammer et al. in prep.). Here we mainly focus on the iron (Fe) and magnesium (Mg) absorption features in the rest-frame UV and their blueshifts, which indicate the presence of cold outflowing gas. In addition, we independently reanalyzed the properties of NS\_274, which are presented in Wu (2025), and incorporated information from the sodium doublet NaI D at rest-frame optical wavelengths. The spectra and photometry analyzed in this work are available online<sup>1</sup>.

Throughout this work, we make use of the AB system to report magnitudes (Oke & Gunn 1983). We adopt a  $\Lambda$  cold dark matter cosmology with  $\Omega_m = 0.3$ ,  $\Omega_\Lambda = 0.7$ , and  $H_0 = 70 \text{ km s}^{-1} \text{ Mpc}^{-1}$ .

## 2. Data

### 2.1. Imaging

NS\_274<sup>2</sup> lies behind the galaxy cluster PLCK G165.7+67.0 at  $z = 0.35$  (G165 in brief). This field was imaged as part of the JWST Prime Extragalactic Areas for Reionization and Lensing Science (PEARLS) guaranteed time observations (Program ID, PID, 1176, PI: R. Windhorst). Follow-up Near Infrared Camera

<sup>1</sup> [10.5281/zenodo.15518189](https://doi.org/10.5281/zenodo.15518189)

<sup>2</sup> The spectroscopic follow-up was primarily designed to characterize the multiply lensed supernova SN H0pe presented in Frye et al. (2024). For our target, we adopt the name it has in this work.

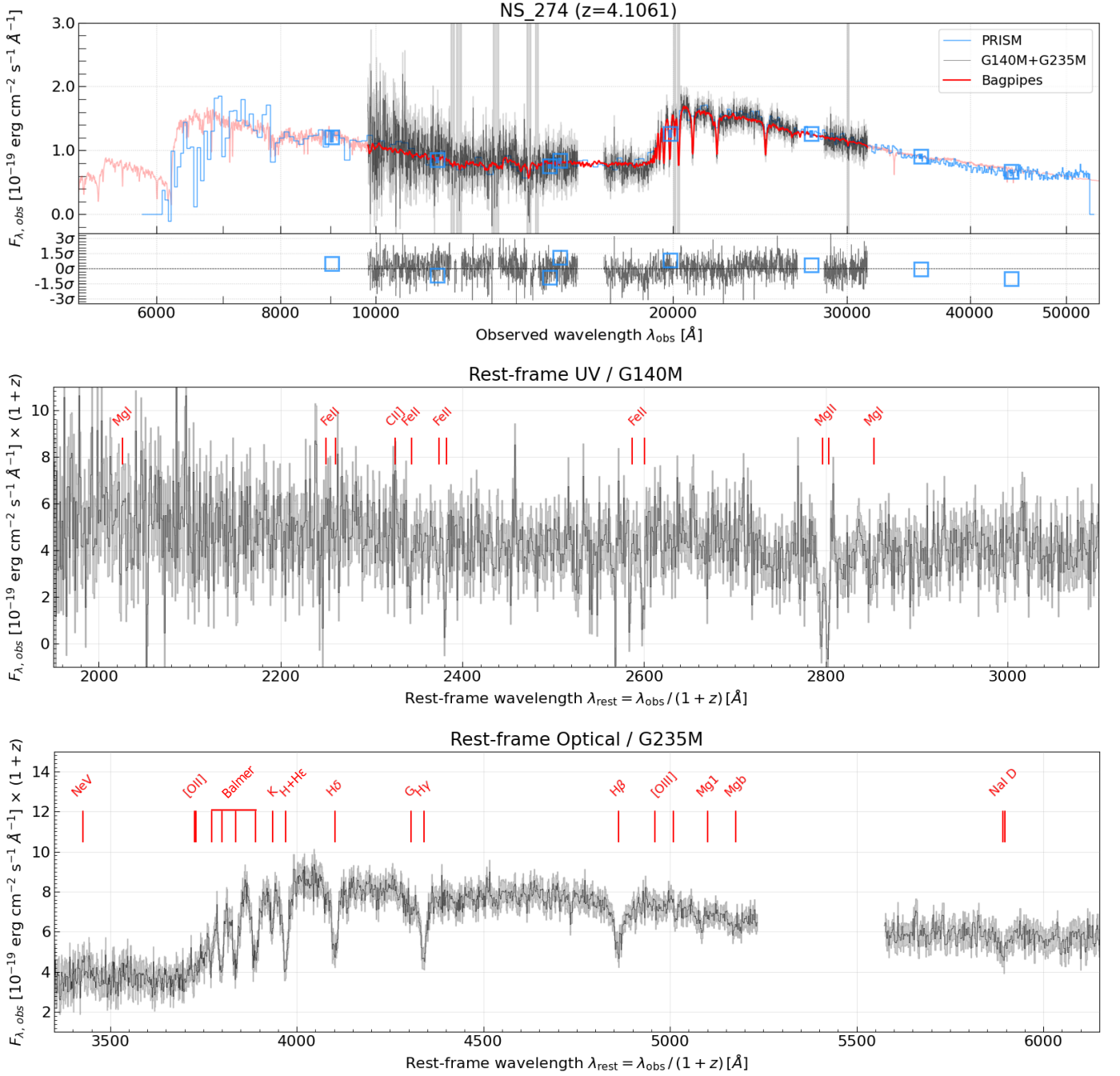


Fig. 2: Spectra, photometry, and SED modeling of NS\_274 at  $z = 4.1061 \pm 0.0003$ . *Top*: Photometry (blue squares), JWST/NIRSpec medium resolution spectra (G140M+G235M, black line), and their uncertainties (gray line) that we jointly modeled with BAGPIPES (red line) in the observed frame. The normalized residuals of the modeling are shown in the lower inset. For reference, we also show the PRISM spectrum (blue). *Center*: Rest-frame UV spectrum covered by the G140M grating. *Bottom*: Rest-frame optical spectrum covered by the G235M grating. We mark in red the expected location of emission and absorption lines at the derived systemic redshift,  $z_{\text{spec}} = 4.1061$ , as labeled. The flux densities in the bottom panels have been rescaled by  $(1+z)$  to conserve the energy.

(NIRCam; Rieke et al. 2023) imaging and Near Infrared Spectrograph (NIRSpec, Jakobsen et al. 2022; Ferruit et al. 2022) spectroscopy was acquired in a JWST disruptive Director’s Discretionary Time program (PID 4446; PI: B. Frye; see Frye et al. 2024 for the analysis of all JWST observations in this field). This field also benefits from ample ancillary data, such as infrared imaging with the Wide Field Camera 3 (WFC3) onboard the *Hubble* Space Telescope (HST) (GO-14223; PI: B. Frye, Frye et al. 2019), Very Large Array (VLA) observations (Pas-

cale et al. 2022), *XMM-Newton* observations (AO22, #92030; PI: B. Frye), and large ground-based telescope observations (see Frye et al. 2024; Kamienieski et al. 2024 for a full description; Cañameras et al. 2018 for previous work on this field). For the purpose of this work, we utilized the available JWST and HST imaging in 8 bands covering the 0.9–4.4  $\mu\text{m}$  range. The images were retrieved from the DAWN JWST Archive (DJA)<sup>3</sup> and ho-

<sup>3</sup> <https://dawn-cph.github.io/dja/index.html>



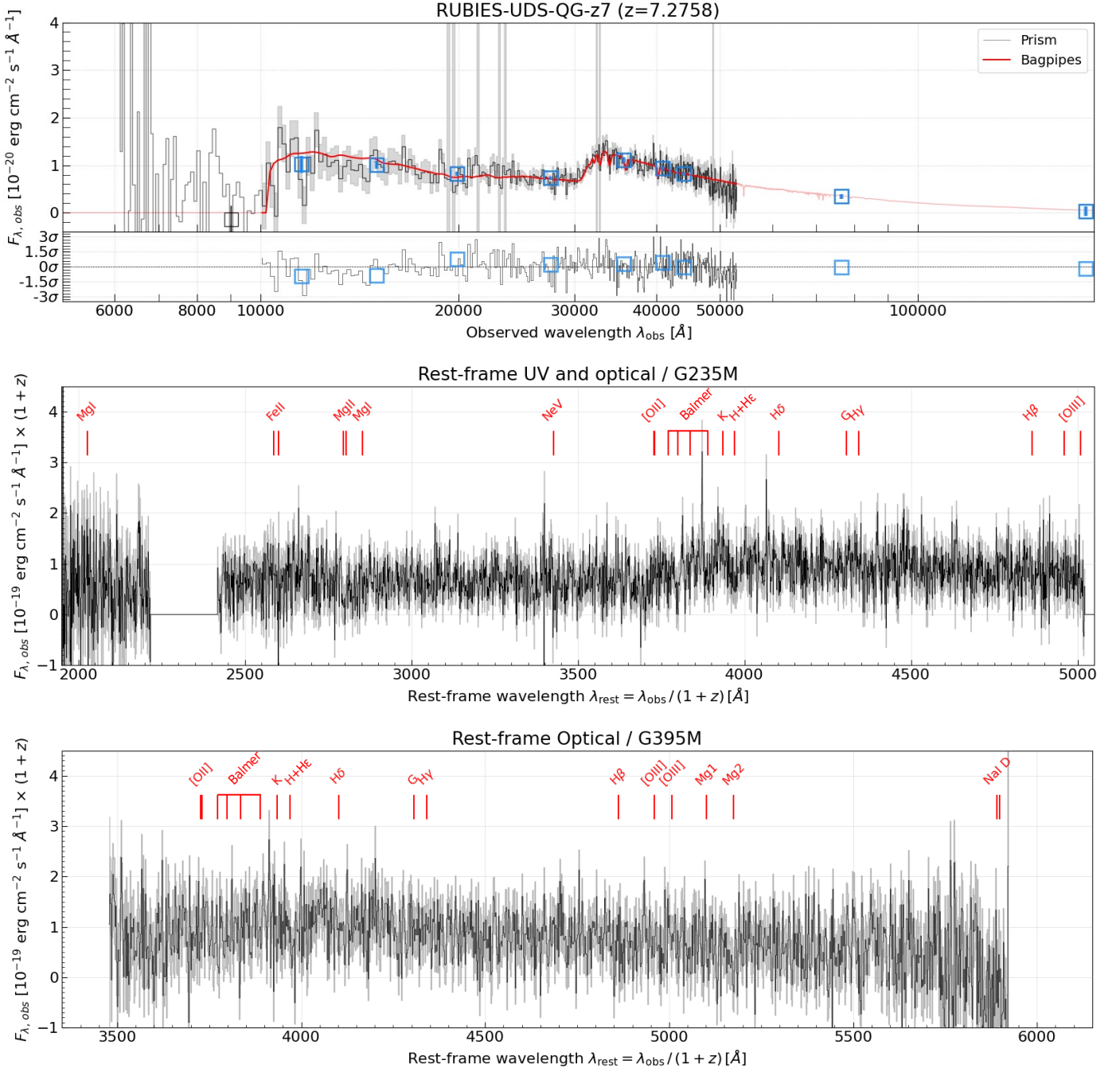


Fig. 3: Spectra, photometry, and SED modeling of RUBIES-UDS-QG-z7 at  $z = 7.2758 \pm 0.0011$ . *Top*: Photometry (blue squares), the JWST/NIRSpec PRISM spectrum (black line), and its uncertainty (gray line) that we jointly modeled with BAGPIPES (red line) in the observed frame. The normalized residuals of the modeling are shown in the lower inset. *Center*: Rest-frame UV spectrum covered by the extended G235M grating. *Bottom*: Rest-frame optical spectrum covered by the G395M grating. We mark in red the expected location of emission and absorption lines at the derived systemic redshift,  $z_{\text{spec}} = 7.2758$ , as labeled. The flux densities in the bottom panels have been rescaled by  $(1+z)$  to conserve the energy.

homogeneously reduced with GRIZLI (Brammer 2023) as described in Valentino et al. (2023). The photometry was extracted from a combined image (mosaic version v7.0) of the available NIRCcam long-wavelength filters in circular apertures (0.5" diameter) with the pythonic version of SourceExtractor (Bertin & Arnouts 1996; Barbary 2016) and corrected to total within an elliptical Kron aperture (Kron 1980). The aperture correction was computed on the combined long wavelength image and applied to all bands

(Valentino et al. 2023). Moreover, we corrected for the minimal extinction of the Milky Way ( $E(B-V) = 0.0165$ ) based on the maps in Schlafly & Finkbeiner (2011). For reference, the observed magnitude in the F200W filter ( $m_{\text{F200W,AB}} = 23.34 \pm 0.05$ ) is consistent with previously reported estimates (Frye et al. 2024; Wu 2025). Finally, we checked for the gravitational lensing effect of the cluster at the location of NS\_274, finding a mild magnification correction of  $\mu = 2.0 \pm 0.2$  in the recent maps

by Kamieneski et al. (2024) – without strongly distorting the shape.<sup>4</sup>

In addition to optical and near-infrared imaging, we obtained coverage of NS\_274 at 1.3 mm (260  $\mu\text{m}$  rest-frame) with the NOEMA Extended Millimetre Array (NOEMA; ID: W23CU001, PIs: Gómez-Guijarro & Valentino). The target was observed for 11.6 hours from May to September 2024 in D configuration. The frequency tunings are 212.5–220.0 GHz in the lower sideband and 228–235.5 GHz in the upper sideband. We reduced and calibrated the data using the GILDAS pipeline at the IRAM headquarters in Grenoble. We produced  $uv$  visibility tables and performed analysis in the  $uv$  space, following the methods described in Jin et al. (2019, 2022, 2024). The clean continuum image was produced using the GILDAS HOGBOM clean routine. The final data product reaches a continuum sensitivity of 33  $\mu\text{Jy}$  at a central frequency of 224 GHz. The resulting synthesized beam is  $1''.85 \times 1''.80$ , and thus the source is unresolved. We do not detect the dust continuum emission from NS\_274. We thus placed a  $3\sigma$  upper limit on its observed flux density of  $\mu F_{260\mu\text{m, rest}} \leq 0.1$  mJy (over a beam, considering that the source is unresolved). We show in Fig. 1 a red-green-blue (RGB) image of NS\_274<sup>5</sup>, where we overlay the contours of the dust continuum emission recorded with NOEMA.

RUBIES-UDS-QG-z7 falls in the footprint of the Public Release IMAGING for Extragalactic Research program (PRIMER; PID 1837, PI: J. Dunlop) in the UDS field. In this case, we made use of the available JWST NIRCам and Mid-Infrared Instrument (MIRI) imaging (v7.2) available on DJA and covering the 0.9 – 18  $\mu\text{m}$  interval. For consistency with the analysis in Weibel et al. (2025), we adopted their total photometry, extracted in  $0''.32$  diameter apertures in point-spread-function-(PSF)-matched images, then corrected for aperture effects and the extinction of our Galaxy. The procedure is detailed in Weibel et al. (2024), to which a custom extraction of the MIRI photometry in  $0''.5$  diameter apertures in the F770W and F1800W images has been added. We note that following a procedure similar to that employed for NS\_274 returns fluxes  $\sim 20\%$  fainter without introducing any significant color differences, thus not appreciably affecting the results of this paper.

## 2.2. Spectroscopy

JWST/NIRSpec Micro-Shutter Array (MSA) spectra of sources in the G165 cluster field were obtained with the PRISM/CLEAR (0.7 – 5.3  $\mu\text{m}$ ,  $R \approx 20 - 300$ ), medium resolution gratings G140M/F100LP (0.9 – 1.8  $\mu\text{m}$ ,  $R \approx 1000$ ), and G235M/F170LP (1.6 – 3.2  $\mu\text{m}$ ,  $R \approx 1000$ ) on April 22, 2023 (PID 4446, PI: B. Frye). The science exposure times were 4420s, 6696s, and 919s for G140M/F100LP, G235M/F170LP, and the PRISM/CLEAR observations, respectively (Frye et al. 2024). NS\_274 was among the targeted sources. The spectra were acquired with a three-microshutter configuration and a three-nod nodding pattern. Also in this case, we retrieved the spectra from the DJA (version v3). These were reduced with the MSAEXP pipeline (Brammer 2024) along the same lines detailed in Heintz et al. (2025) and de Graaff et al. (2025a). The current public version of MSAEXP includes updated reference files and improves on the absolute and color-dependent flux calibration and the bar shadow correction. The spectra were optimally extracted

(Horne 1986) and their noise budget conservatively scaled up such that the residuals of a wavelength-dependent polynomial model subtracted to the spectrum are normally distributed, as expected for pure background integrations (although localized noise correlation due to the line spread function could induce deviations from this assumption). This corresponds to a  $\sim 25\%$ ,  $25\%$ , and  $45\%$  noise median increase for the PRISM, G140M, and G235M spectra. Finally, we anchored the spectra to the total photometry as derived in Sect. 2.1 to correct for residual slit losses. We applied a fourth-order polynomial correction to the spectra, which resulted in slowly varying rescaling on the order of 5–40%, the most extreme correction being at the very blue end of the PRISM spectrum. The results are robust against the choice of alternative scaling functions (spline and Chebyshev polynomials) and the degree of the polynomial (a simple constant or parabolic functional form already corrects for most of the offset between the spectra and the total photometry). The photometry and spectra of NS\_274 are shown in Fig. 2.

NIRSpec/MSA spectra of RUBIES-UDS-QG-z7 were obtained on July 25, 2024, with PRISM/CLEAR and G395M/F290LP as part of the Red Unknowns: Bright Infrared Extragalactic Survey survey (RUBIES, PID 4233, PIs: A. de Graaff & G. Brammer; de Graaff et al. 2025a). Both spectra were acquired with 2880s combined integrations with a three-microshutter configuration and a three-nod nodding pattern. These spectra were reduced following the same steps as detailed above. The photometry and PRISM spectrum of RUBIES-UDS-QG-z7 are shown in Fig. 3. The G395M spectrum does not show any appreciable absorption features at high enough S/N (Weibel et al. 2025), which resulted in relatively loose initial redshift constraints ( $z = 7.29 \pm 0.01$ ).

On July 23, 2024, a G235M/F170LP spectrum was also obtained as part of the “DeepDive” survey (PID 3567, PI: F. Valentino; Ito et al. in prep.). A similar nodding pattern was used also in this case, but leaving three extra shutters open for an optimal background subtraction. The total integration time was of 10,590 s. The G235M/F170LP grating was processed with a customized version of MSAEXP (v4) that allowed us to recover the whole wavelength range permitted by the combination of the F170LP long-pass filter and projection on the detector (Brammer et al. in prep.). The distributed JWST pipeline automatically cuts the red end of the grating spectra to avoid contamination of the primary first spectral order with higher orders, which appear at predictable locations and intensities (Jakobsen et al. 2022). However, by extending the wavelengthrange<sup>6</sup> pipeline reference file and calibrating the intensities of the second and third order spectra (which include the full response of the telescope, the shape of the filters, and flat-fielding, all summarized in a revised sensitivity curve), the full spectrum recorded on the detector can be recovered. The sensitivity curve extending beyond the nominal coverage of the filter (1.6–3.2  $\mu\text{m}$ ) was derived from the wavelength and flux commissioning and calibration programs COM PIDs 1125 (PI: J. Muzerolle Page) and 1128 (PI: N. Luetzgendorf) and CAL PID 1538 (PI: K. Gordon). This allowed us to extend the spectrum up to 4.2  $\mu\text{m}$ , now crucially covering the full Balmer break (Fig. 3). The normalization and continuum shape of the extended G235M/F170LP spectrum are consistent with those of the G395M/F290LP spectrum in the overlapping regions without introducing any further corrections. Given the intrinsic red spectrum of the target and the decreasing trans-

<sup>4</sup> We note that this target is outside the field of view of the lensed image constraints used in the models (Frye et al. 2024).

<sup>5</sup> The image was produced with TRILOGY by D. Coe, <https://github.com/dancoe/Trilogy>

<sup>6</sup> [https://jwst-pipeline.readthedocs.io/en/latest/jwst/references\\_general/wavelengthrange\\_reffile.html](https://jwst-pipeline.readthedocs.io/en/latest/jwst/references_general/wavelengthrange_reffile.html)

mission of the G235M disperser at  $\lambda \gtrsim 2.3 \mu\text{m}$ , the uncertainties on the flux calibration after modeling the contamination of the higher order spectra are comparable with the errors on the standard absolute calibration. In addition, the extended G235M spectrum has an approximately 1.7 times higher spectral resolution than G395M at a given wavelength where they overlap. Finally, to avoid spurious systematics when comparing our analysis with that of [Weibel et al. \(2025\)](#), we anchored both the extended G235M and the G395M spectra to their PRISM data. In this case, the median noise rescaling amounts to 10% and 50% for the PRISM and G235M, respectively, and no appreciable difference for G395M<sup>7</sup>.

### 3. Methods

#### 3.1. Spectrophotometric modeling

##### 3.1.1. NS\_274

Initially, we re-derived the systemic redshift of NS\_274 by modeling the stellar absorption features in the rest-frame optical probed by the G235M grating (Fig. 2). We did so with the Penalized PiXel Fitting (pPXF) code ([Cappellari & Emsellem 2004](#)) and following an approach similar to that in [Cappellari \(2023\)](#). We used models from the Flexible Stellar Population Synthesis (FSPS) library ([Conroy & Gunn 2010](#)) normalized around the rest-frame optical V-band. We ran the code twice: we initially masked regions potentially contaminated by emission lines, then identified and excluded  $3\sigma$  outlier pixels, and reran the modeling. We allowed only for multiplicative fourth-order polynomials as correction factors to the overall shape of the spectrum, but this choice did not affect the robustness of the redshift solution ( $z_{\text{spec}} = 4.1061 \pm 0.0003$ , which is slightly lower than, but consistent with, the  $z = 4.1076 \pm 0.0023$  first reported in Table 2 of [Frye et al. 2024](#)) and of the stellar velocity dispersion estimate. We derived a value of  $\sigma_{\star} = 255^{+39}_{-42} \text{ km s}^{-1}$  by modeling the stellar absorption features in the spectrum, excluding deep Balmer lines ( $H\beta$ ,  $H\gamma$ , and  $H\delta$ ) and other portions of the wavelength range possibly impacted by strong emission lines ([O III] and [O II]). We corrected this estimate for the wavelength-dependent instrumental resolution, which we assumed was a factor of 1.3 higher than the nominal resolving power ([de Graaff et al. 2025a](#)). Finally, we attempted to add an ionized gas component typically responsible for the emission of bright rest-frame optical emission lines (e.g., Balmer lines, [O II], and [O III]), but we did not retrieve any meaningful detections. We thus place upper limits on the emission lines fluxes covered by the G235M grating by assuming a line width identical to that of the stellar absorption<sup>8</sup> (see [Übler et al. 2024](#) and references therein for a recent discussion on this assumption). These values are reported in Table 1. The uncertainties are derived by bootstrapping the spectrum 500 times and repeating the modeling procedure.

Once the systemic redshift was determined, we simultaneously modeled NIRC2 and WFC3 photometry and the combined NIRS2 grating data using BAGPIPES ([Carnall et al. 2018, 2020](#)). We masked spectral regions potentially contaminated by the absorption of the interstellar medium (iron and

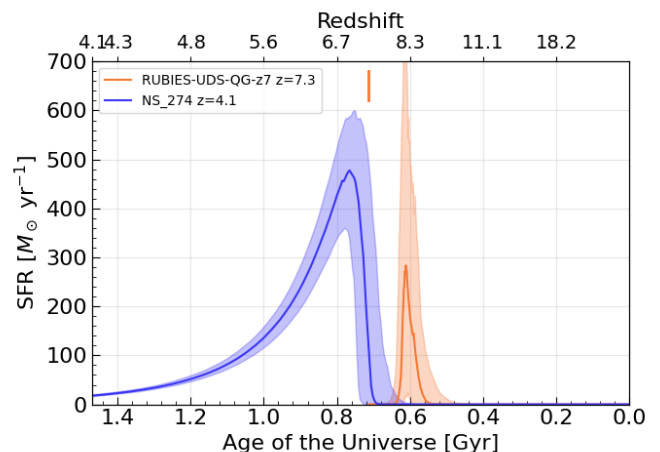


Fig. 4: SFHs of our targets. We show the best-fit double power-law SFHs of RUBIES-UDS-QG-z7 (orange) and NS\_274 (blue) and their uncertainties. The age of the Universe is truncated at the observed redshift of NS\_274. The orange segment marks the observed redshift of RUBIES-UDS-QG-z7.

magnesium lines in the rest-frame UV, the calcium and sodium doublets in the optical). We adopted [Bruzual & Charlot \(2003\)](#) stellar population synthesis models, the parameterization of the dust attenuation law in [Salim et al. \(2018\)](#), with fixed UV bump amplitude,  $B = 1$ , and slope deviation from a [Calzetti et al. 2000](#) law,  $\delta = -0.2$ , for a shape similar to that in [Kriek & Conroy 2013](#), and a default [Kroupa & Boily \(2002\)](#) initial mass function (IMF). We adopted a double-power law star formation history (SFH), which offers enough flexibility to capture a fast rise and decline of the star formation rate (SFR) in the past. We fixed the value of the stellar velocity dispersion to  $\sigma_{\star} = 255 \text{ km s}^{-1}$ . The adopted priors and their shapes are collected in Table B.1 and shown in Fig. B.2. The fitted data and best model are shown in Fig. 2, while we report best-fit parameters of interest in Table 1. A corner plot with the posterior distributions of such parameters is shown in Appendix B.1. We tested these results against the use of looser priors, different parameterizations of the SFHs (e.g., lognormal and delayed  $\tau$ -models), and a different code (Fast++; [Schreiber et al. 2018b](#)). We also attempted to model the photometry, grating, and PRISM independently or combined. Finally, we explored the effect of the imposed priors on the final estimates of interesting physical quantities at test. We found the best-fit estimates to be consistent across this range of tests and robust against the choice of the priors. Predictably, the range of parameter estimates obtained under different assumptions is larger than what implied by the statistical uncertainties with a single set of priors and premises (see [Pacifci et al. 2023](#) for a comparative study of systematic effects in spectral energy distribution modeling). As an example, these tests provide  $M_{\star}$  estimates varying within a  $\sim 0.2$  dex range encompassing our fiducial values in Table 1.

Accounting for the magnification effect ( $\mu = 2.0 \pm 0.2$ ), we estimate an intrinsic stellar mass of  $\sim 4 \times 10^{10} M_{\odot}$ . The spectral energy distribution (SED) modeling suggests that NS\_274 underwent a short and intense (peak  $\mu\text{SFR} \sim 500 M_{\odot} \text{ yr}^{-1}$ ) growth spurt approximately  $\sim 500$  Myr prior to the time of observations, leaving behind some modest level of SFR over the last 100 Myr (intrinsic  $\text{SFR}_{100 \text{ Myr}} = 10.7^{+0.1}_{-0.1} M_{\odot} \text{ yr}^{-1}$ ) and 10 Myr

<sup>7</sup> At this point, the reader might wonder about the extension of the spectra of NS\_274. We briefly describe their content and limitations in Appendix A.

<sup>8</sup> See Appendix A for an attempt to measure emission lines in the extended G235M spectrum.

Table 1: Measurements and physical properties.

Property	NS_274	RUBIES-UDS-QG-z7
R.A. [deg]	171.8236199	34.4296173
Decl. [deg]	42.4696455	-5.1122962
$z_{\text{spec}}$	$4.1061 \pm 0.0003$	$7.2758 \pm 0.0011$
$\mu$	$2.0 \pm 0.2$	1
$\mu$ [Ne III] $\lambda$ 3870 [ $10^{-19}$ cgs]	$2.4^{+2.8}_{-2.4}$	—
$\mu$ [O II] $\lambda$ 3729 [ $10^{-19}$ cgs]	$< 6.6$	—
$\mu$ H $\beta$ $\lambda$ 4863 [ $10^{-19}$ cgs]	$8.0^{+3.7}_{-3.8}$	—
$\mu$ [O III] $\lambda$ 5008 [ $10^{-19}$ cgs]	$8.9^{+3.9}_{-4.2}$	—
$\mu$ $m_{\text{F200W,AB}}$ [mag]	$23.34 \pm 0.05$	$26.31 \pm 0.06$
$\log(M_{\star}/M_{\odot})$	$10.57^{+0.02}_{-0.02}$	$10.13^{+0.07}_{-0.02}$
$A_V$ [mag]	$0.40^{+0.04}_{-0.04}$	$0.50^{+0.06}_{-0.10}$
$\text{SFR}_{100\text{Myr}}$ [ $M_{\odot} \text{ yr}^{-1}$ ]	$10.7^{+0.1}_{-0.1}$	$33^{+93}_{-32}$
$\text{SFR}_{10\text{Myr}}$ [ $M_{\odot} \text{ yr}^{-1}$ ]	$9.0^{+0.1}_{-0.1}$	$< 2$
$\text{SFR}_{\text{IR}, 8-1000\mu\text{m}}$ [ $M_{\odot} \text{ yr}^{-1}$ ]	$< 12$	—
$\text{SFR}_{[\text{OII}]}$ [ $M_{\odot} \text{ yr}^{-1}$ ]	$< 0.4$	—
$\text{SFR}_{\text{H}\beta}$ [ $M_{\odot} \text{ yr}^{-1}$ ]	$1.5^{+0.7}_{-0.7}$	—
$\log(\text{sSFR}_{100\text{Myr}}/\text{yr}^{-1})$	$-9.54^{+0.05}_{-0.05}$	$-8.7^{+0.6}_{-1.9}$
$\sigma_{\star}$ [km s $^{-1}$ ]	$255^{+39}_{-42}$	—
$\Delta v_{\text{off}}$ [km s $^{-1}$ ]	$-182 \pm 50$	$-169 \pm 46$
$R_{\text{maj}}$ [pc]	$262^{+17}_{-15}$	$209^{+33}_{-24}$
$n_{\text{Sersic}}$	$6.5^{+0.6}_{-0.5}$	$2.4^{+1.5}_{-0.9}$
$\log(M_{\text{dyn}}/M_{\odot})$	$10.18^{+0.13}_{-0.16}$	—
$\log(N(\text{FeII})/\text{cm}^{-2})$	$15.00 \pm 0.19$	—
$\log(N(\text{MgII})/\text{cm}^{-2})$	$15.35 \pm 0.74$	$\sim 17.9$
$\log(N(\text{NaI})/\text{cm}^{-2})$	$12.15 \pm 0.59$	—
$\log(N(\text{H}_{\text{Fe}})/\text{cm}^{-2})$	$21.19 \pm 0.19$	—
$\log(N(\text{H}_{\text{Mg}})/\text{cm}^{-2})$	$20.57 \pm 0.74$	$\sim 23.1$
$\log(N(\text{H}_{\text{Na}})/\text{cm}^{-2})$	$19.79 \pm 0.59$	—
$\dot{M}_{\text{out}}$ [ $M_{\odot} \text{ yr}^{-1}$ ] (Fe, Mg, Na)	$(5^{+5}_{-3}, 1^{+7}_{-1}, 0.2^{+0.8}_{-0.2})$	$(-, \sim 269, -)$
$\eta$ (Fe, Mg, Na)	$(0.2^{+0.3}_{-0.1}, 0.1^{+0.4}_{-0.1}, 0.01^{+0.04}_{-0.01})$	$(-, \sim 12, -)$

**Notes.** Upper limits at  $3\sigma$ . The [Ne III], [O II], H $\beta$ , and [O III] fluxes refer to emission lines obtained after subtracting the underlying stellar continuum.  $\dot{M}_{\text{out}}$  and  $\eta$  are computed assuming  $v_{\text{out}} = \Delta v_{\text{off}}$  and  $\text{SFR}_{100\text{Myr}}$  (Sect. 4 for a discussion of alternative options).

( $\text{SFR}_{10\text{Myr}} = 9.0^{+0.1}_{-0.1} M_{\odot} \text{ yr}^{-1}$ ; Fig. 4). We also constrain the dust obscured SFR by rescaling a modified black body with dust temperature  $T_{\text{dust}} = 35$  K and  $\beta$  slope of 1.8 (Witstok et al. 2023) to the upper limit on the continuum emission at  $260 \mu\text{m}$  rest-frame, while accounting for the effect of the cosmic microwave background (da Cunha et al. 2013). The resulting  $\text{SFR}_{\text{IR}, 8-1000\mu\text{m}}$ , using the conversion in Kennicutt (1998) adapted for our assumed IMF and corrected for the magnification factor, is  $< 12 M_{\odot} \text{ yr}^{-1}$  (at the  $3\sigma$  level). This value is consistent with the estimate from the modeling of the shorter wavelength SED, also characterized by a low estimate of  $A_V$ . The absence of strong [O II], [O III], and H $\beta$  emission further constrains the more recent SFR on shorter timescales of 10 Myr. It also implies the absence of a bright AGN radiating efficiently (e.g., [O III]/H $\beta$  =  $1.1^{+1.2}_{-0.5}$ ; but see Appendix A and Wu 2025 for caveats and limits on faint and radia-

tively inefficient AGN activity). Table 1 reports the constraints on SFR from the emission lines assuming the conversion in Kennicutt (1998) for H $\beta$  and Kewley et al. (2004) for [O II], correcting for the dust attenuation for the stellar continuum from the SED modeling and for the assumed IMF. These constraints place NS\_274 in a post-starburst phase, as also supported by the deep stellar Balmer absorption lines. Estimates of the Lick indices ( $\text{H}\gamma_{\text{A}} = 6.91 \pm 0.80 \text{ \AA}$  and  $\text{H}\delta_{\text{A}} = 7.83 \pm 0.75 \text{ \AA}$ , Worthey & Ottaviani 1997) and of the  $D_n4000$  index ( $D_n4000 = 1.25 \pm 0.02$ , Balogh et al. 1999), computed following the procedure detailed in Gallazzi et al. 2014, are indeed typical of post-starburst systems in the local Universe.



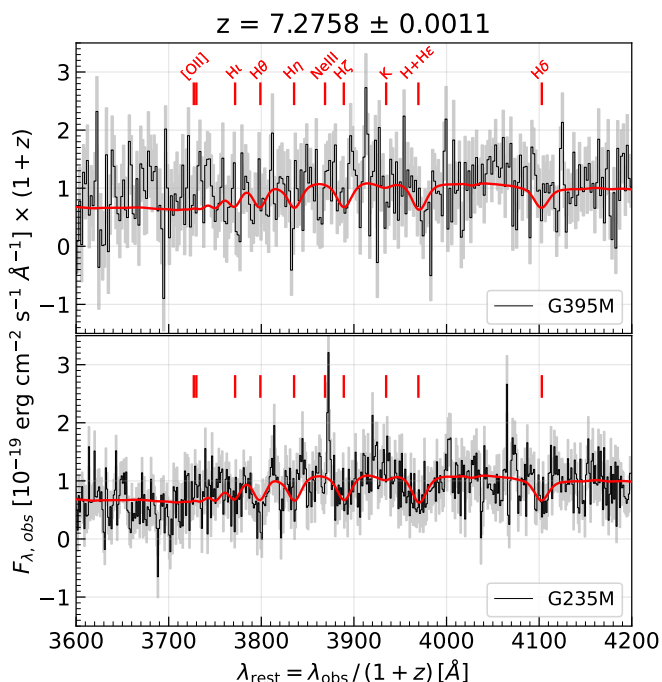


Fig. 5: Zoomed-in view of the Balmer break region of RUBIES-UDS-QG-z7 in the G395M spectrum from Weibel et al. (2025, *top*) and our extended G235M spectrum (*bottom*). The black and gray lines show the data and their uncertainties. The red lines indicate the best-fit model (Sect. 3.1.2). The red ticks indicate the most notable absorption features, as labeled.

### 3.1.2. RUBIES-UDS-QG-z7

The extended G235M spectrum shows absorption features that are not visible in the G395M spectrum (Fig. 5). While the depth of the spectrum does not allow for a robust estimate of the stellar velocity dispersion from these lines, a collective model of their wavelengths tightly constrains the redshift. To combine the information from both the G235M and G395M spectra at their respective resolutions, we proceeded as follows. We ran pPXF with a similar setting as for NS\_274 on the extended G235M spectrum. We then took the best-fit template at its intrinsic resolution and simultaneously fitted it to both the G235M and G395M spectra, convolving the model to their corresponding resolution curves. We allowed for a normalization rescaling for each spectrum, but the shape of the template was fixed. The remaining free parameters were the redshift and the velocity dispersion. The fitting procedure was implemented using EMCEE (Foreman-Mackey et al. 2013), where we assumed a Gaussian likelihood and flat priors. The best-fit model is shown in Fig. 5, corresponding to  $z = 7.2758 \pm 0.0011$ , which is consistent with the PRISM-based determination. The corner plot with the posterior distributions of the free parameters is shown in Fig. B.3. As noted, the velocity dispersion is poorly constrained, which is why it was not considered any further in the analysis.

For consistency with the work by [Weibel et al. \(2025\)](#), we opted for modeling the PRISM spectrum and photometry with BAGPIPES using the same set of assumptions as for our fiducial model of NS\_274, but fixing the redshift to our revised estimate. The best-fit parameters (Table 1) and the overall shape of the SFHs are broadly consistent with those reported in [Weibel et al. \(2025\)](#). The modeled data and the best-fit models are

shown in Fig. 3. Also in this case, the modeling suggests that RUBIES-UDS-QG-z7 experienced a short and vigorous main formation burst (peak SFR  $\sim 200 M_{\odot} \text{ yr}^{-1}$ ) approximately  $\sim 150$  Myr prior to the observed redshift, immediately followed by an abrupt suppression of the SFR ( $\text{SFR}_{100 \text{ Myr}} = 33^{+93}_{-32} M_{\odot} \text{ yr}^{-1}$  and  $\text{SFR}_{10 \text{ Myr}} < 2 M_{\odot} \text{ yr}^{-1}$  at  $3\sigma$ ; Fig. 4). As noted in the past (de Graaff et al. 2025b), the unconstrained stellar metallicity does have an impact on the reconstructed SFH and SFR estimates. In this case, the preferred solution ( $Z \sim 0.5Z_{\odot}$ ) is in between the low- ( $\sim 0.1Z_{\odot}$ ) and high- $Z$  ( $\sim Z_{\odot}$ ) models in Weibel et al. (2025). On shorter timescales, the upper limit on the emission lines set a constraint on the SFR of  $\lesssim 6 M_{\odot} \text{ yr}^{-1}$  (Weibel et al. 2025).

### 3.2. Modeling the rest-frame UV and optical absorption features tracing outflowing neutral gas

A few rest-frame UV absorption lines tracing the presence of neutral gas from low-ionization elements in galaxies (Mg II doublet at  $\lambda\lambda 2796, 2803$ ; Fe II at  $\lambda\lambda 2586, 2600$ ; 2374, 2383) are robustly detected in the G140M spectrum of NS\_274 (Fig. 6). Absorption features at similar redshifts are also at least tentatively detected (e.g., Mg I at  $\lambda 2853$ ). In the rest-frame optical covered by the G235M grating, we also robustly detect the Na I  $\lambda\lambda 5891, 5897$  doublet in absorption (Na I D, although blended at this resolution), indicating an additional dense component in the neutral gas-phase. Common to all these features is a blueshift compared to the systemic redshift derived from the well-detected stellar absorption features, indicating a substantial column of outflowing gas in the line of sight. In the case of RUBIES-UDS-QG-z7, given the limited S/N and coverage, we are only able to robustly detect the presence of Mg II (Fig. 6).

To explore the properties of the outflowing gas, we consistently modeled these absorption features with VoigtFit (Krogager 2018)<sup>9</sup> following the approach in Heintz et al. (2023). The code models the lines with Voigt profiles at the delivered spectral resolution and returns the column densities,  $N$ , and broadening parameters,  $b$ , due to thermal and turbulent motions for an arbitrary number of velocity components. Since absorption from stars and the interstellar medium (or even emission from the latter) can arise at the systemic redshift (Sugahara et al. 2017; Man et al. 2021; Davies et al. 2024), when modeling the lines in the spectra of NS\_274, we implemented a two-component model, with one at fixed  $z = z_{\text{spec}}$ . We also ran the code iteratively: a first pass with free broadening parameter and velocity offsets,  $\Delta v_{\text{off}}$ , to determine the latter, followed by a second iteration at fixed parameters to derive the column densities of the outflowing component. However, given the available resolving power ( $R \approx 1000$ ) and depth, the final estimates of  $N$  are affected by significant uncertainties (Table 1). The same conditions also limit more refined modeling of stellar population in the rest-frame UV (Maltby et al. 2019), which we thus leave for future work with better data quality (but see Wu 2025 for an attempt). When simultaneously modeling the Fe, Mg, and Na transitions, we tied their broadening parameter and velocity structure, assuming that they physically trace the bulk of the neutral gas-phase in galaxies. Considering that the ionization potentials of the elements considered here (Na 5.1 eV, Fe 7.9 eV, Mg 7.6 eV) are comparable and lower than that of hydrogen (13.6 eV), this assumption is physically motivated. Finally, we note that, in principle,  $\log(N(\text{MgII}))$  might be underestimated due to saturation of the line core. Given the

<sup>9</sup> <https://github.com/jkrogager/VoigtFit>



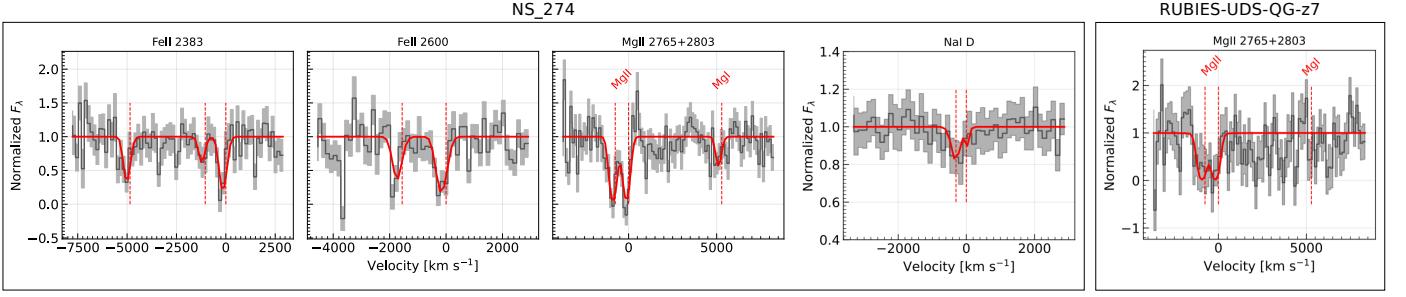


Fig. 6: Blueshifted absorption features. Left panels: Continuum-normalized spectrum (black line) and its uncertainties (gray line) around FeII, MgII+MgI, and NaI D lines for NS\_274. Rightmost panel: G235M spectrum around MgII+MgI for RUBIES-UDS-QG-z7. The best-fit model with VoigtFit is marked by the solid red line. The systemic velocity for each line is marked by dashed red lines.

limited information in the spectra of RUBIES-UDS-QG-z7, we did not attempt a two-component model and fixed  $b = 100 \text{ km s}^{-1}$ , which is consistent with the results for NS\_274. We caution the reader that this might lead to an underestimate of the velocity offset and of  $\log(N)$ . Deeper and higher resolution spectra will help address several of these issues in the future.

The best-fit models obtained with VoigtFit are shown in Fig. 6. We derive an average velocity offset of the absorbing gas of  $\Delta v_{\text{off}} = -182 \pm 50 \text{ km s}^{-1}$  and  $-169 \pm 46 \text{ km s}^{-1}$  for NS\_274 and RUBIES-UDS-QG-z7, respectively, with tails extending up to a few hundred  $\text{km s}^{-1}$ . In the case of NS\_274, the velocity structure is derived from the joint modeling of the MgII, MgI, FeII, and NaI lines mentioned above, and the offset is consistent with the estimate first reported in Wu (2025). However, the wavelength shifts of each line are consistent. These results indicate that the dominant neutral gas column is associated with the outflowing gas. The estimated column densities are reported in Table 1. We converted  $\log(N(\text{FeII}))$ ,  $\log(N(\text{MgII}))$ , and  $\log(N(\text{NaI}))$  into  $\log(N_{\text{H}})$ , assuming a gas-phase metallicity and empirical depletion patterns, under the same assumptions detailed in Wu (2025):

$$\log(N_{\text{H}}) = \log(N_{\text{X}}) - \delta_{\text{depl}, \text{X}} - \log(N_{\text{X}}/N_{\text{H}})_{\odot} - \log(Z/Z_{\odot}), \quad (1)$$

where  $X = \text{Fe, Mg, and Na}$ ;  $\delta_{\text{depl}, \text{X}}$  is the metal depletion onto dust ( $\delta_{\text{Fe}} = -1.7$ ,  $\delta_{\text{Mg}} = -0.8$  are the median values in the Galactic disk (Jenkins 2009); and  $\delta_{\text{Na}} = -0.95$  is the canonical estimate for the Milky Way from Savage & Sembach 1996);  $\log(N_{\text{X}}/N_{\text{H}})_{\odot}$  are the solar abundance patterns for Fe (-4.49), Mg (-4.42), and Na (-5.69, Savage & Sembach 1996); and  $Z$  the metallicity of the targets. We included a neutral fraction correction of a factor of ten for NaI, but this number could be substantially higher in the extreme conditions of a recent burst of star formation or AGN activity at high redshifts (Veilleux et al. 2020). We do not apply any ionization corrections for Fe and Mg, assuming that the singly ionized ions are the dominant population. This allows us to draw a direct comparison with the analysis in Wu (2025) without introducing major systematics. For reference, we assume  $Z = Z_{\odot}$ . The values from our spectrophotometric modeling are consistent with it, but they are a source of major uncertainty. This is particularly true for RUBIES-UDS-QG-z7, whose high redshift would suggest a metallicity lower than and an abundance pattern different from solar (Weibel et al. 2025).

Finally, we note that, at this stage, the velocity offset can in principle be interpreted as due to a genuine neutral gaseous out-

flow or from a cloud intervening gas along the line of sight. However, this second possibility is disfavored by the absence of credible galaxies associated with the putative absorbers along the line of sight in the surrounding of our targets. Moreover, the implied high column densities (Sect. 4) require a non-negligible level of metal enrichment, and thus underlying stellar mass, which is not detected (although low surface brightness galaxies that fall below the flux limit cannot be ruled out).

### 3.3. Structural properties

Morphological properties for RUBIES-UDS-QG-z7 were derived in Weibel et al. (2025) using the Bayesian code PYSERVIC (Pasha & Miller 2023)<sup>10</sup>. The authors retrieve an effective semimajor axis of  $R_{\text{maj}} = 209^{+33}_{-24} \text{ pc}$  for a rather round shape (axis ratio of  $R_{\text{min}}/R_{\text{maj}} = 0.89^{+0.08}_{-0.14}$ , where  $R_{\text{min}}$  is the semiminor axis) and a relatively low, but poorly constrained, Sérsic (1968) index of  $n = 2.4^{+1.5}_{-0.9}$ . We followed a similar procedure and modeled the emission of NS\_274 in the F200W band using the same code. The choice of the band is a compromise between mapping relatively long wavelengths ( $\sim 4000 \text{ \AA}$  rest frame) at the highest possible resolution (sampled with a  $0''.02$  pixel scale) and S/N. We built a PSF model by broadening the profile derived with WEBBPSF (Perrin et al. 2014) to match the width of observed unsaturated stars in the field, as described in Ito et al. (2024). We modeled a single Sérsic (1968) profile. The source is resolved: we estimate an effective semimajor axis of  $R_{\text{maj}} = 262^{+17}_{-15} \text{ pc}$  and a high  $n = 6.5^{+0.6}_{-0.5}$  index. We applied an average  $\mu^{-0.5}$  correction to the effective size to account for the mild lensing effect. Nevertheless, this correction does not substantially alter the conclusions of this work. The source is slightly elongated (ellipticity  $\epsilon = 1 - R_{\text{min}}/R_{\text{maj}} = 0.49^{+0.02}_{-0.02}$ ). We show the best-fit model and the residuals in Appendix B. These results are consistent with the analysis with GALFIT (Peng et al. 2002) in Wu (2025), once the lensing correction is accounted for.

Combined with the stellar velocity dispersion, we estimated the dynamical mass expected for NS\_274 as

$$M_{\text{dyn}} = K(n) K(q) \sigma_{\star}^2 R_{\text{maj}} / G, \quad (2)$$

where  $K(n) = 8.87 - 0.831n + 0.0241n^2$  depends on the Sérsic index  $n$  (Cappellari et al. 2006),  $K(q) = (0.87 + 0.38e^{-3.78(1-q)})^2$  depends on the projected axis ratio  $q$  (van der Wel et al. 2022),  $R_{\text{maj}}$  is the semimajor axis, and  $G$  is the gravitational constant. After accounting for the lensing effect,  $\log(M_{\star}/M_{\odot}) = 10.57^{+0.02}_{-0.02}$

<sup>10</sup> <https://github.com/pysersic/pysersic>

is higher than, but in overall agreement with,  $\log(M_{\text{dyn}}/M_{\odot}) = 10.18^{+0.13}_{-0.16}$ , especially considering the numerous assumptions on the stellar population and dynamical modeling behind each of these calculations and the typical systematic uncertainties ( $\sim 0.2$  dex on the stellar mass).

#### 4. Outflow properties

At this point we had ascertained the presence of Mg II (and in the case of NS\_274 also Mg I, Fe II, and Na I D) blueshifted absorption features in the spectra of two post-starburst, recently quenched galaxies at high redshifts.

How much gas is outflowing from these galaxies and at what rate? Adopting the simple spherical thin-shell model in Wu (2025) and Davies et al. (2024), we derived the outflowing mass  $M_{\text{out}}$  and its rate  $\dot{M}_{\text{out}}$  as

$$\begin{aligned} M_{\text{out}} &= 1.4 m_p \Omega N(\text{H}) R_{\text{out}}^2, \\ \dot{M}_{\text{out}} &= 1.4 m_p \Omega N(\text{H}) R_{\text{out}} v_{\text{out}}, \end{aligned} \quad (3)$$

where  $m_p$  is the proton mass,  $\Omega$  the solid angle subtended by the outflow,  $R_{\text{out}}$  the shell radius, and  $v_{\text{out}}$  its velocity (Rupke et al. 2005). We adopt the same approach as in Wu (2025) to directly compare with their results and avoid systematics. We thus assume  $\Omega = 0.45 \times 4\pi$  (based on Davies et al. 2024),  $R_{\text{out}} = 2R_{\text{maj}}$ , and  $v_{\text{out}} = \Delta v_{\text{off}}$  is the average outflow velocity from our fit (Table 1). For NS\_274, we obtain  $\log(M_{\text{out}}/M_{\odot}) = 7.4^{+0.2}_{-0.3}$ ,  $6.8^{+0.7}_{-0.9}$ , and  $6.0^{+0.6}_{-0.7}$  from Fe, Mg, and Na, respectively. The estimate based on Fe is in good agreement with that reported in Wu (2025,  $\log(M_{\text{out}}/M_{\odot}) \sim 7.8$ ), while that derived from Mg is  $\sim 10\times$  larger. The outflow mass from Fe and Mg are in agreement, while that from Na is lower by  $\sim 1$  dex at face value. This might be due to the fact that the observed transitions, while broadly tracing the neutral hydrogen phase of the ISM, are sensitive to gas conditions, with Na I D preferentially being a proxy of the colder and denser gas. For RUBIES-UDS-QG-z7, we derive  $\log(M_{\text{out}}/M_{\odot}) \sim 9.1$  from Mg, based on a column density of  $\log(N(\text{MgII})/\text{cm}^{-2}) \sim 17.9$ . These estimates are more uncertain than those derived for NS\_274 (largely due to the assumption on  $b$ , the absence of S/N to constrain Fe lines, and a systemic component) and their face values should be taken with a grain of salt. The derived HI column density is remarkably high (Table 1) and, if confirmed, its effects could be tested in deeper PRISM data around the Lyman limit (e.g., Heintz et al. 2025).

We estimate mass outflow rates of  $\dot{M}_{\text{out}} \sim 0.2 - 5 M_{\odot} \text{ yr}^{-1}$  and  $\sim 269 M_{\odot} \text{ yr}^{-1}$  for NS\_274 and RUBIES-UDS-QG-z7, respectively. The range in  $\dot{M}_{\text{out}}$  for NS\_274 reflects the difference in  $\log(N(\text{H}))$  from Na and Fe. The high column density from Mg dominates this high, albeit uncertain, estimate of  $\dot{M}_{\text{out}}$  for RUBIES-UDS-QG-z7. The corresponding mass loading factors are  $\eta = \dot{M}_{\text{out}}/\text{SFR} \sim 0.01 - 0.2$  and  $\sim 12$  for NS\_274 and RUBIES-UDS-QG-z7, where we adopted the SFR averaged over the last 100 Myr for the calculation. The estimates of  $\dot{M}_{\text{out}}$  and  $\eta$  linearly depend on  $v_{\text{out}}$ , and the mass loading factor is also sensitive to the value of the SFR. On the one hand, adopting the alternative assumption of  $v_{\text{out}} = \Delta v_{\text{off}} + 2\sigma$ , where  $\sigma$  is the velocity dispersion of the outflow absorption feature (e.g., Davies et al. 2024), we would obtain  $\dot{M}_{\text{out}}$  and  $\eta$  estimates  $1.8\times$  higher for both targets, given our modeling of the outflow velocity structure with fixed  $b = 100 \text{ km s}^{-1}$  and assuming pure

Doppler broadening ( $b = \sqrt{2}\sigma$ ). We stress that higher resolution observations are necessary to properly constrain  $b$  and break its degeneracy with the column densities. On the other hand, assuming an estimate of SFR averaged on shorter timescales, would have a lesser effect on the estimate of  $\eta$  for NS\_274 at fixed  $v_{\text{out}}$  (SFR<sub>100Myr</sub> is  $\sim 20\%$  higher than SFR<sub>10Myr</sub>, Table 1). Instead, it would boost even further  $\eta$  for RUBIES-UDS-QG-z7 (the  $3\sigma$  upper limit of SFR<sub>10Myr</sub>  $< 2 M_{\odot} \text{ yr}^{-1}$  would correspond to a lower limit on  $\eta$  more than ten times higher than that derived assuming SFR<sub>100Myr</sub>). The choice of a shorter timescale is also consistent with the expected time that an outflow would take to reach our reference scale of  $R_{\text{out}} = 2R_{\text{maj}}$  with a constant  $v_{\text{out}} = \Delta v_{\text{off}}$  ( $\sim 2.5$  Myr for both targets).

#### 5. Discussion

##### 5.1. Outflow velocities in recently quenched galaxies across time

In Fig. 7 we show the average outflow velocities  $v_{\text{out}}$  as a function of  $M_{\star}$ , SFR, and SFR surface density ( $\Sigma_{\text{SFR}} = \text{SFR}/(2\pi R_{\text{eff}}^2)$ ) for samples of star-forming and post-starburst galaxies up to  $z \sim 1.5 - 2$  based on the large literature compilation in Davis et al. (2023). In this case, we considered outflows predominantly traced by Mg and Fe absorption to minimize the systematics in the comparison (see Sun et al. 2024 for an analysis of outflows traced by Na I D in local post-starburst galaxies). Interestingly, in terms of average outflow velocities, the neutral gas outflows in NS\_274 and RUBIES-UDS-QG-z7 are broadly consistent with those observed in local star-forming and post-starburst galaxies at fixed  $M_{\star}$ , SFR, or  $\Sigma_{\text{SFR}}$ . The velocity offsets measured in two lensed recently quenched systems at  $z \sim 3$  in Man et al. (2021) and in the stacked spectra of post-starburst galaxies at  $1 < z < 1.4$  in Maltby et al. (2019) are also shown for reference. In both cases, they are also consistent with the correlations observed at lower redshifts.

The fact that the average velocities detected in NS\_274 and RUBIES-UDS-QG-z7 at high redshift are overall consistent with those observed in nearby post-starburst galaxies seems to suggest that the mechanisms launching them during or shortly after quenching are similar to those operating in the local Universe. This is best captured in the tightest among the correlations, the one between  $v_{\text{out}}$  and  $\Sigma_{\text{SFR}}$  (Heckman et al. 2015). In this case, the typically higher SFRs at fixed stellar masses at high redshift are balanced by an increasing compactness, so that the launch of winds via copious star formation occurring in small volumes, as one could expect to detect in early galaxies immediately after quenching, is consistent with that observed in rarer, similarly massive systems at low redshift. However, only larger samples of recently quenched galaxies at  $z > 2 - 3$  will tell us if this is the case, or if a bona fide evolution of the  $v_{\text{out}} - \Sigma_{\text{SFR}}$  (and  $M_{\star}$ , SFR) relations exists (Sugahara et al. 2017).

We also note that the scaling relations considered here do not include any explicit terms to account for possible AGN activity. Interestingly, samples specifically selected or consistent with post-starburst galaxies shown in Fig. 7 do not show evident signs of ongoing powerful AGN activity (Maltby et al. 2019; Davis et al. 2023; the sources in Man et al. 2021 may host faint Type II AGNs based on their [O III]/[O II] ratios). According to our analysis, this is the case also for the galaxies analyzed here (but see Appendix A and Wu 2025). Taken together, this suggests that ongoing AGN activity is not necessarily required to explain the average outflow velocities of NS\_274,

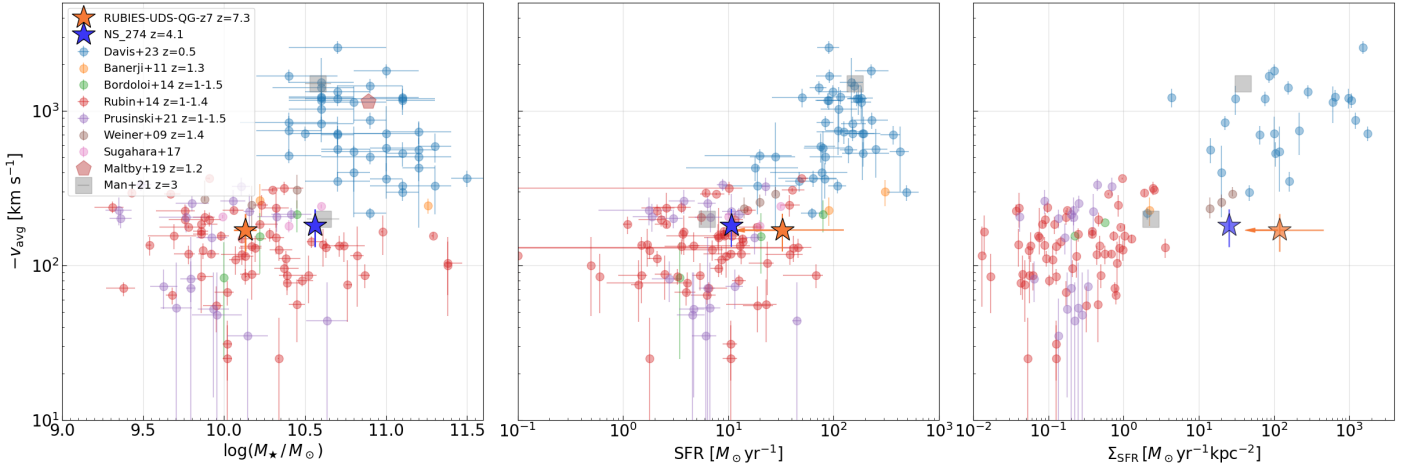


Fig. 7: Average outflow velocity as a function of the stellar mass,  $\text{SFR}_{100\text{Myr}}$ , and surface density of  $\text{SFR}_{100\text{Myr}}$  (corrected by the magnification factor for NS\_274). Filled stars indicate the targets analyzed in this work. The colored filled circles represent the homogenized literature compilation of Mg II outflows across redshifts from Davis et al. (2023, and references therein). The results from the stacking of post-starburst galaxies at  $z \sim 1.2$  from Maltby et al. (2019) are shown with a red pentagon. The locations of two  $z \sim 3$  recently quenched sources in Man et al. (2021) are marked by gray squares.

RUBIES-UDS-QG-z7, but also lower-redshift post-starburst galaxies in Fig. 7 at fixed  $M_*$ , SFR, or  $\Sigma_{\text{SFR}}$ .

## 5.2. Outflow masses, loading factors, and energetics

If the outflows in NS\_274 and RUBIES-UDS-QG-z7 show velocities similar to those observed in more local post-starburst systems at fixed  $M_*$ , SFR and  $\Sigma_{\text{SFR}}$  without invoking any strong AGN contribution, the simple calculations in Sect. 4 depict a partially different scenario, at least for RUBIES-UDS-QG-z7.

## 5.3. Outflows as relics of the star formation process winding down in NS\_274

For NS\_274, we find that the mass loading factor  $\eta = \dot{M}_{\text{out}}/\text{SFR} = 0.01 - 0.2$  and the energy associated with the outflow ( $\dot{E}_{\text{out}} = 0.5 \dot{M}_{\text{out}} v_{\text{out}}^2 \sim 0.2 - 5 \times 10^{40} \text{ erg s}^{-1}$ ) are consistent with basic expectations for SNe-powered outflows, where the minimum and maximum values of these ranges are derived from the estimates of  $N(\text{NaI})$  and  $N(\text{FeII})$ , respectively (Table 1). To show this, we adopt the approach in Veilleux et al. (2005). Based on the Starburst99 (Leitherer et al. 1999) models with solar metallicity and a Salpeter (1955) IMF, we expect an injection of energy due to SNe on the order of  $\dot{E}_{\text{SN}} = 7 \times 10^{41} \times \text{SFR}_{100\text{Myr}} = (7.5 \pm 0.1) \times 10^{42} \text{ erg s}^{-1}$  and a mass outflow rate  $\dot{M}_{\text{SN}} = 0.26 \times \text{SFR}_{100\text{Myr}} = (2.8 \pm 0.1) M_{\odot} \text{ yr}^{-1}$ . Even neglecting a simple linear scaling to match the IMF of our choice and assuming coupling with the ISM on the order of  $\sim 10\%$  or less, the injected energy is broadly consistent with our empirical estimate for NS\_274. This holds also assuming  $\text{SFR}_{10\text{Myr}}$  and  $v_{\text{out}} = \Delta v_{\text{off}} + 2\sigma$  for the calculation ( $\dot{E}_{\text{out}} \propto v_{\text{out}}^3$ , thus 5.6 times higher than in the case of  $v_{\text{out}} = \Delta v_{\text{off}}$ ). Similarly, the mass outflow rate is in agreement with our observational estimate ( $\dot{M}_{\text{out}} = 0.2 - 5 M_{\odot} \text{ yr}^{-1}$ , Table 1). Taken with the findings described in the previous section, it seems that the levels of star formation over the last  $\sim 10$ -100 Myr are sufficient to explain the properties of the outflows observed in NS\_274 (Fig. 4). However, given the slow average outflow velocity ( $\Delta v_{\text{off}} \sim 180 \text{ km s}^{-1}$ , lower than the stellar velocity dispersion ( $\sigma_{\star} \sim 250 \text{ km s}^{-1}$ ),

and the mass loading factor  $\eta \lesssim 1$ , it is unlikely that the observed outflows are responsible for the quenching of star formation in NS\_274.

## 5.4. Extreme outflow properties might indicate undetected AGN activity in RUBIES-UDS-QG-z7

The very large value of  $\eta > 10$  and  $\dot{E}_{\text{out}} \sim 2 \times 10^{42} \text{ erg s}^{-1}$  for RUBIES-UDS-QG-z7 give leeway to different interpretations. The mass outflow rate from Mg II ( $\dot{M}_{\text{out}} \sim 269 M_{\odot} \text{ yr}^{-1}$  for  $v_{\text{out}} = \Delta v_{\text{off}}$ ,  $1.8\times$  higher for a less conservative assumption on  $v_{\text{out}}$ ; Sect. 4) largely exceeds the value expected from SNe-driven winds ( $\dot{M}_{\text{SN}} = 9_{-8}^{+24}$  and  $< 0.5 M_{\odot} \text{ yr}^{-1}$  assuming  $\text{SFR}_{100\text{Myr}}$  and  $\text{SFR}_{10\text{Myr}}$ , respectively), suggesting a contribution from other ejective mechanism, i.e., powered by an AGN. The injected energy is broadly consistent with  $\dot{E}_{\text{SN}} = 2_{-2}^{+6} \times 10^{43} \text{ erg s}^{-1}$  considering a 10% coupling with the ISM only by assuming  $\text{SFR}_{100\text{Myr}}$  and  $v_{\text{out}} = \Delta v_{\text{off}}$  as representative, and the agreement is largely due to the loose constraints on the recent SFR estimate. In fact, adopting  $v_{\text{out}} = \Delta v_{\text{off}} + 2\sigma$  would increase  $\dot{E}_{\text{out}}$  by a factor of  $\sim 6$  and  $\text{SFR}_{10\text{Myr}}$  would set an upper limit on  $\dot{E}_{\text{SN}} < 10^{42} \text{ erg s}^{-1}$ . The findings for RUBIES-UDS-QG-z7 are, thus, more consistent with those obtained from mapping the neutral gas outflows using the sodium NaI D tracer in recently quenched galaxies at  $z = 2 - 3$ , carrying large amount of gas masses and energies away from galaxies (Belli et al. 2024; Davies et al. 2024), as simulations and models postulate, despite the absence of clear ongoing AGN activity.

## 5.5. Caveats and future perspectives

Combined with recent findings on outflows and galaxy quenching in the literature, our results for NS\_274 and RUBIES-UDS-QG-z7 contribute to describing this phenomenon as being as rich and complex as it is in the local Universe, despite the much shorter time frame in which it can occur. However, a few words of caution are due.



First, we stress that the measurements and simple calculations in the previous sections are affected by significant uncertainties and rely on several assumptions. As an example, in the case of NS\_274, the mass loading factor derived in this work significantly differs from the range presented in Wu (2025,  $\eta \sim 7 - 30$ ), which drives us to different conclusions about the origin of the observed outflows. The disparity is mainly ascribable to the SFR estimate to compute  $\eta$ . Different assumptions in the modeling of the spectrophotometric data of NS\_274 lead to different SFR estimates than presented in Wu (2025). Moreover, as noted in Sect. 4, adopting SFRs averaged over 10 Myr or 100 Myr periods gives an idea of the expected systematic uncertainties on  $\eta$  and the rest of the physical quantities depending on these parameters. While the time necessary for an outflow moving at  $v_{\text{out}} = \Delta v_{\text{off}}$  to reach  $R_{\text{out}}$  would suggest to employ 10 Myr averaged SFRs, a timescale of 100 Myr is on the lower end of the lifespan of outflows in the galaxy halos as suggested by observational and theoretical studies (Davis et al. 2023, and references therein). The choice of  $\text{SFR}_{100\text{Myr}}$  also allows us to directly compare our findings with those in the literature compilation shown in Fig. 7. Together with the analysis of the origin of possible faint emission lines in the optical rest-frame spectrum and the mild lensing correction, this is where our analysis of NS\_274 mainly differs from that presented in Wu (2025, see also our Appendix A).

Second, definitive proof of the effect of AGN and stellar feedback on their hosts remains hard to constrain even with exquisite data and under consistent assumptions, given the widely different spatial and temporal scales of several competing processes involved. In particular, extreme outflow properties (e.g., velocities, masses, and energies) can be somewhat more confidently associated with the action of AGNs than to SNe, even in absence of typical signatures such as high optical line ratios or broad lines in their spectra, as in the case of RUBIES-UDS-QG-z7. This is because of the short-term AGN variability (i.e., the imprint of an AGN on outflows can outlast its presence and detectability in recently quenched galaxies) and the fact that the feedback mode that quenches star-formation in galaxies can be characterized by low Eddington ratios in some models (Lagos et al. 2025, even if this is still matter of debate Choi et al. 2017; De Lucia et al. 2024; Farcy et al. 2025). The variability and radiative inefficiency play also a role in the case of less extreme outflows conditions, such as those we reconstructed for NS\_274 and similarly found in normal star-forming galaxies. While in principle consistent with the energy, momentum, and mass provided by SN feedback, low values of these quantities do not exclude a significant contribution from AGNs a priori, especially for galaxy-scale outflows and for those models where gas entrainment in the circumgalactic medium plays a major role (Mitchell et al. 2020).

Promising approaches to countering the effect of the short-term AGN variability rely on proxies of the integrated, rather than instantaneous, effect of the growth of supermassive black holes (e.g., their masses; Bluck et al. 2023) on their host galaxies. Valid attempts tested in the local Universe (e.g., Wang et al. 2024) are now extended to high-redshift samples (see the discussions in Ito et al. 2025; Baker et al. 2025; Onoue et al. 2024). Tying these properties with those of outflows in larger samples of galaxies similar to those presented here will be key to attenuate the effect of different spatial and temporal scales, and to obtain a more decisive evidence of how stellar and black hole masses grow and coevolve from star-forming to quiescent

phases.

## 6. Conclusions

We have reported the detection of signatures of outflowing gas in the rest-UV and optical JWST/NIRSpec spectra of two massive ( $M_{\star} \sim 10^{10.2} M_{\odot}$ ) and recently quenched galaxies: NS\_274 at  $z = 4.1061$  and RUBIES-UDS-QG-z7 at  $z = 7.2758$ . New observations with the G235M grating, reduced with a customized version of the MSAEXP pipeline, allowed us to ascertain the redshift of RUBIES-UDS-QG-z7, which had previously only been constrained by low-resolution PRISM data. The presence of gas outflows is revealed by blueshifted ionized magnesium, iron, and neutral sodium absorption features, which trace the neutral hydrogen phase. Our analysis of the spectra of these galaxies allowed us to reach the following conclusions.

- Both targets show signatures typical of recently quenched star formation. The absence of strong emission lines and the reconstructed SFHs from spectrophotometric modeling predict low SFRs on short (10 Myr) and intermediate (100 Myr) scales ( $\text{SFR}_{100\text{Myr}} \sim 15 M_{\odot} \text{ yr}^{-1}$ ). The quiescence of NS\_274 is further confirmed by the lack of strong dust continuum emission, which allows us to set an upper limit on the obscured SFR of  $< 12 M_{\odot} \text{ yr}^{-1}$ .
- The measured outflow velocities ( $\sim 180 \text{ km s}^{-1}$ ) are consistent with those measured in post-starburst galaxies nearby ( $z \lesssim 0.7$ ) and up to  $z \sim 1 - 3$  at fixed  $M_{\star}$ , SFR, and  $\Sigma_{\text{SFR}}$  without strong signatures of ongoing AGN activity. This suggests that outflows in galaxies quenched on short timescales are powered by similar mechanisms across cosmic time. This can be tested by tracing these scaling relations at  $z \gtrsim 2 - 3$  (in particular, the tightest one:  $v_{\text{out}} - \Sigma_{\text{SFR}}$ ) with large spectroscopic samples of recently quenched systems.
- Under simple assumptions, we derive outflow masses, rates, loading factors, and energetics for both galaxies – finding them to be rather different. For NS\_274 at  $z = 4.1$ , benefiting from higher quality spectra, we find values that are in principle consistent with predictions for SN-powered outflows over timescales of 10-100 Myr. However, low values of the mass loading factor ( $\eta \lesssim 1$ ) and velocities indicate that it is unlikely that the observed outflows are responsible for the star formation quenching.
- For RUBIES-UDS-QG-z7, the extreme mass loading factor ( $\eta > 10$ ) suggests the contribution of an undetected AGN as a powering mechanism for the observed outflow. Interestingly, this is not reflected in an extremely high average outflow velocity. In fact, the observational estimate is consistent with that recorded for the outflow in NS\_274 and in local post-starburst galaxies with similar  $M_{\star}$ , SFR, and/or  $\Sigma_{\text{SFR}}$  values.
- Maybe more importantly, these case studies prove that it is possible to detect neutral outflowing gas in distant ( $z > 4$ ) post-starburst galaxies via Mg and Fe in the rest-frame UV, and Na in the optical, even with relatively inexpensive integrations of a handful of hours with medium resolution gratings with JWST/NIRSpec. The logical next step is to construct larger samples to test scaling relations as a function of cosmic time and compare outflow properties with model predictions for instantaneous and integrated SN and AGN feedback; such work would mitigate the effect of the wide range of spatial and temporal scales involved in galaxy quenching.

## Data availability

The calibrated spectra and photometry are available via doi: [10.5281/zenodo.15518189](https://doi.org/10.5281/zenodo.15518189). The specific JWST and HST observations analyzed can be obtained from the Mikulski Archive for Space Telescopes at the Space Telescope Science Institute and accessed via doi: [10.17909/3ev1-rx30](https://doi.org/10.17909/3ev1-rx30).

**Acknowledgements.** We thank the referee for their insightful comments that improved this article. FV warmly thanks Christy Tremonti for providing the measurements for the literature sample shown in Fig. 7. FV is also indebted to Carlos Gómez-Guijarro, the co-principal investigator of the NOEMA program, for many years of stimulating and fruitful scientific discussions on the topics presented in this work – and for his valued friendship. This work is based in part on observations made with the NASA/ESA/CSA James Webb Space Telescope. The data were obtained from the Mikulski Archive for Space Telescopes at the Space Telescope Science Institute, which is operated by the Association of Universities for Research in Astronomy, Inc., under NASA contract NAS 5-03127 for JWST. The observations are associated with programs # 1176, 1837, 3567, 4233, and 4446. Support for program # 3567 was provided by NASA through a grant from the Space Telescope Science Institute, which is operated by the Association of Universities for Research in Astronomy, Inc., under NASA contract NAS 5-03127. This work is also based on observations carried out under project number W23CU with the IRAM Interferometer NOEMA. IRAM is supported by INSU/CNRS (France), MPG (Germany) and IGN (Spain). We are grateful for the help received from IRAM staff during observations and data reduction. FV is grateful for the support of the Japanese Society for the Promotion of Science through the Fellowship (JSPS) S23108 and for the hospitality of Masayuki Tanaka and his group at the National Observatory of Japan, where part of this work has been conducted. Some of the data products presented herein were retrieved from the Dawn JWST Archive (DJA). DJA is an initiative of the Cosmic Dawn Center, which is funded by the Danish National Research Foundation under grant DNR140. FV, KI, and PZ acknowledge support from the Independent Research Fund Denmark (DFF) under grant 3120-00043B. KEH acknowledges support from the Swiss State Secretariat for Education, Research and Innovation (SERI) under contract number MB22.00072. SJ and GEM acknowledges the Villum Fonden research grants 37440 and 13160. MF and MH acknowledge funding from the Swiss National Science Foundation (SNF) via a PRIMA Grant PR00P2 193577 “From cosmic dawn to high noon: the role of black holes for young galaxies”. PFW acknowledges funding through the National Science and Technology Council grants 113-2112-M-002-027-MY2. This study was also supported by JSPS KAKENHI Grant Numbers JP22J00495, JP23K13141, and JP25K07361.

## References

- Antwi-Danso, J., Papovich, C., Esdaile, J., et al. 2025, *ApJ*, 978, 90
- Baker, W. M., Lim, S., D’Eugenio, F., et al. 2025, *MNRAS*, 539, 557
- Baldwin, J. A., Phillips, M. M., & Terlevich, R. 1981, *PASP*, 93, 5
- Balogh, M. L., Morris, S. L., Yee, H. K. C., Carlberg, R. G., & Ellingson, E. 1999, *ApJ*, 527, 54
- Barbary, K. 2016, *The Journal of Open Source Software*, 1, 58
- Baron, D., Netzer, H., Davies, R. I., & Xavier Prochaska, J. 2020, *MNRAS*, 494, 5396
- Baron, D., Netzer, H., Lutz, D., Prochaska, J. X., & Davies, R. I. 2022, *MNRAS*, 509, 4457
- Belli, S., Park, M., Davies, R. L., et al. 2024, *Nature*, 630, 54
- Bertin, E. & Arnouts, S. 1996, *A&AS*, 117, 393
- Bluck, A. F. L., Piotrowska, J. M., & Maiolino, R. 2023, *ApJ*, 944, 108
- Brammer, G. 2023, *grizli*
- Brammer, G. 2024, *msaexp: NIRS spec analysis tools*
- Bruzual, G. & Charlot, S. 2003, *MNRAS*, 344, 1000
- Cañameras, R., Nesvadba, N. P. H., Limousin, M., et al. 2018, *A&A*, 620, A60
- Calzetti, D., Armus, L., Bohlin, R. C., et al. 2000, *ApJ*, 533, 682
- Cappellari, M. 2023, *MNRAS*, 526, 3273
- Cappellari, M., Bacon, R., Bureau, M., et al. 2006, *MNRAS*, 366, 1126
- Cappellari, M. & Emsellem, E. 2004, *PASP*, 116, 138
- Carnall, A. C., Cullen, F., McLure, R. J., et al. 2024, *MNRAS*, 534, 325
- Carnall, A. C., McLure, R. J., Dunlop, J. S., & Davé, R. 2018, *MNRAS*, 480, 4379
- Carnall, A. C., McLure, R. J., Dunlop, J. S., et al. 2023, *Nature*, 619, 716
- Carnall, A. C., Walker, S., McLure, R. J., et al. 2020, *MNRAS*, 496, 695
- Choi, E., Ostriker, J. P., Naab, T., et al. 2017, *ApJ*, 844, 31
- Coil, A. L., Weiner, B. J., Holz, D. E., et al. 2011, *ApJ*, 743, 46
- Conroy, C. & Gunn, J. E. 2010, *ApJ*, 712, 833
- da Cunha, E., Groves, B., Walter, F., et al. 2013, *ApJ*, 766, 13
- Davies, R. L., Belli, S., Park, M., et al. 2024, *MNRAS*, 528, 4976
- Davis, J. D., Tremonti, C. A., Swiggum, C. N., et al. 2023, *ApJ*, 951, 105
- de Graaff, A., Brammer, G., Weibel, A., et al. 2025a, *A&A*, 697, A189
- de Graaff, A., Setton, D. J., Brammer, G., et al. 2025b, *Nature Astronomy*, 9, 280
- De Lucia, G., Fontanot, F., Xie, L., & Hirschmann, M. 2024, *A&A*, 687, A68
- D’Eugenio, C., Daddi, E., Gobat, R., et al. 2020, *ApJ*, 892, L2
- D’Eugenio, F., Pérez-González, P. G., Maiolino, R., et al. 2024, *Nature Astronomy*, 8, 1443
- Farcy, M., Hirschmann, M., Somerville, R. S., et al. 2025, *MNRAS* (submitted), arXiv:2504.08041
- Ferruit, P., Jakobsen, P., Giardino, G., et al. 2022, *A&A*, 661, A81
- Foreman-Mackey, D., Hogg, D. W., Lang, D., & Goodman, J. 2013, *PASP*, 125, 306
- Forrest, B., Annunziatella, M., Wilson, G., et al. 2020a, *ApJ*, 890, L1
- Forrest, B., Marsan, Z. C., Annunziatella, M., et al. 2020b, *ApJ*, 903, 47
- Forrest, B., Wilson, G., Muzzin, A., et al. 2022, *ApJ*, 938, 109
- Förster Schreiber, N. M. & Wuyts, S. 2020, *ARA&A*, 58, 661
- Frye, B., Broadhurst, T., & Benítez, N. 2002, *ApJ*, 568, 558
- Frye, B. L., Pascale, M., Pierel, J., et al. 2024, *ApJ*, 961, 171
- Frye, B. L., Pascale, M., Qin, Y., et al. 2019, *ApJ*, 871, 51
- Gallazzi, A., Bell, E. F., Zibetti, S., Brinchmann, J., & Kelson, D. D. 2014, *ApJ*, 788, 72
- Glazebrook, K., Nanayakkara, T., Schreiber, C., et al. 2024, *Nature*, 628, 277
- Glazebrook, K., Schreiber, C., Labbé, I., et al. 2017, *Nature*, 544, 71
- Heckman, T. M., Alexandroff, R. M., Borthakur, S., Overzier, R., & Leitherer, C. 2015, *ApJ*, 809, 147
- Heintz, K. E., Brammer, G. B., Watson, D., et al. 2025, *A&A*, 693, A60
- Heintz, K. E., De Cia, A., Thöne, C. C., et al. 2023, *A&A*, 679, A91
- Horne, K. 1986, *PASP*, 98, 609
- Ito, K., Tanaka, T. S., Shimasaku, K., et al. 2025, *MNRAS*, 538, 1501
- Ito, K., Valentino, F., Brammer, G., et al. 2024, *ApJ*, 964, 192
- Jakobsen, P., Ferruit, P., Alves de Oliveira, C., et al. 2022, *A&A*, 661, A80
- Jenkins, E. B. 2009, *ApJ*, 700, 1299
- Ji, Z., Williams, C. C., Rieke, G. H., et al. 2024, arXiv:2409.17233
- Jin, S., Daddi, E., Magdis, G. E., et al. 2019, *ApJ*, 887, 144
- Jin, S., Daddi, E., Magdis, G. E., et al. 2022, *A&A*, 665, A3
- Jin, S., Sillassen, N. B., Hodge, J., et al. 2024, *A&A*, 690, L16
- Kakimoto, T., Tanaka, M., Onodera, M., et al. 2024, *ApJ*, 963, 49
- Kamienieski, P. S., Frye, B. L., Windhorst, R. A., et al. 2024, *ApJ*, 973, 25
- Kennicutt, Jr., R. C. 1998, *ARA&A*, 36, 189
- Kewley, L. J., Dopita, M. A., Leitherer, C., et al. 2013, *ApJ*, 774, 100
- Kewley, L. J., Geller, M. J., & Jansen, R. A. 2004, *AJ*, 127, 2002
- Kokorev, V., Chisholm, J., Endsley, R., et al. 2024, *ApJ*, 975, 178
- Kriek, M. & Conroy, C. 2013, *ApJ*, 775, L16
- Krogager, J.-K. 2018, arXiv e-prints, arXiv:1803.01187
- Kron, R. G. 1980, *ApJS*, 43, 305
- Kroupa, P. & Boily, C. M. 2002, *MNRAS*, 336, 1188
- Kubo, M., Umehata, H., Matsuda, Y., et al. 2022, *ApJ*, 935, 89
- Kurichi-Vendhan, S., Farcy, M., Hirschmann, M., & Valentino, F. 2024, *MNRAS*, 534, 3974
- Lagos, C. d. P., Valentino, F., Wright, R. J., et al. 2025, *MNRAS*, 536, 2324
- Leitherer, C., Schaerer, D., Goldader, J. D., et al. 1999, *ApJS*, 123, 3
- Maltby, D. T., Almaini, O., McLure, R. J., et al. 2019, *MNRAS*, 489, 1139
- Man, A. W. S., Zabl, J., Brammer, G. B., et al. 2021, *ApJ*, 919, 20
- Merlin, E., Fortuni, F., Torelli, M., et al. 2019, *MNRAS*, 2241
- Mingozzi, M., James, B. L., Arellano-Córdova, K. Z., et al. 2022, *ApJ*, 939, 110
- Mitchell, P. D., Schaye, J., Bower, R. G., & Crain, R. A. 2020, *MNRAS*, 494, 3971
- Naab, T. & Ostriker, J. P. 2017, *ARA&A*, 55, 59
- Nanayakkara, T., Glazebrook, K., Jacobs, C., et al. 2024, *Scientific Reports*, 14, 3724
- Oke, J. B. & Gunn, J. E. 1983, *ApJ*, 266, 713
- Onoue, M., Ding, X., Silverman, J. D., et al. 2024, arXiv:2409.07113
- Pacifici, C., Iyer, K. G., Mobasher, B., et al. 2023, *ApJ*, 944, 141
- Pascale, M., Frye, B. L., Dai, L., et al. 2022, *ApJ*, 932, 85
- Pasha, I. & Miller, T. B. 2023, *The Journal of Open Source Software*, 8, 5703
- Peng, C. Y., Ho, L. C., Impey, C. D., & Rix, H.-W. 2002, *AJ*, 124, 266
- Perrin, M. D., Sivaramakrishnan, A., Lajoie, C.-P., et al. 2014, in *Society of Photo-Optical Instrumentation Engineers (SPIE) Conference Series*, Vol. 9143, *Space Telescopes and Instrumentation 2014: Optical, Infrared, and Millimeter Wave*, ed. J. Oschmann, Jacobus M., M. Clampin, G. G. Fazio, & H. A. MacEwen, 91433X
- Rieke, M. J., Kelly, D. M., Misselt, K., et al. 2023, *PASP*, 135, 028001
- Rubin, K. H. R., Prochaska, J. X., Koo, D. C., et al. 2014, *ApJ*, 794, 156
- Rupke, D. S., Veilleux, S., & Sanders, D. B. 2005, *ApJS*, 160, 87
- Rupke, D. S. N., Coil, A., Geach, J. E., et al. 2019, *Nature*, 574, 643
- Salim, S., Boquien, M., & Lee, J. C. 2018, *ApJ*, 859, 11
- Salpeter, E. E. 1955, *ApJ*, 121, 161
- Savage, B. D. & Sembach, K. R. 1996, *ARA&A*, 34, 279
- Schlafly, E. F. & Finkbeiner, D. P. 2011, *ApJ*, 737, 103
- Schreiber, C., Glazebrook, K., Nanayakkara, T., et al. 2018a, *A&A*, 618, A85

- Schreiber, C., Labbé, I., Glazebrook, K., et al. 2018b, A&A, 611, A22
- Sersic, J. L. 1968, Atlas de Galaxias Australes
- Setton, D. J., Khullar, G., Miller, T. B., et al. 2024, ApJ, 974, 145
- Shapley, A. E., Steidel, C. C., Pettini, M., & Adelberger, K. L. 2003, ApJ, 588, 65
- Somerville, R. S. & Davé, R. 2015, ARA&A, 53, 51
- Sugahara, Y., Ouchi, M., Lin, L., et al. 2017, ApJ, 850, 51
- Sun, Y., Lee, G.-H., Zabludoff, A. I., et al. 2024, MNRAS, 528, 5783
- Tanaka, M., Onodera, M., Shimakawa, R., et al. 2024, ApJ, 970, 59
- Tanaka, M., Valentino, F., Toft, S., et al. 2019, ApJ, 885, L34
- Taylor, E., Maltby, D., Almaini, O., et al. 2024, MNRAS, 535, 1684
- Tremonti, C. A., Moustakas, J., & Diamond-Stanic, A. M. 2007, ApJ, 663, L77
- Turner, C., Tacchella, S., D'Eugenio, F., et al. 2025, MNRAS, 537, 1826
- Übler, H., Förster Schreiber, N. M., van der Wel, A., et al. 2024, MNRAS, 527, 9206
- Urbano Stawinski, S. M., Cooper, M. C., Forrest, B., et al. 2024, The Open Journal of Astrophysics, 7, 46
- Valentino, F., Brammer, G., Gould, K. M. L., et al. 2023, ApJ, 947, 20
- Valentino, F., Tanaka, M., Davidzon, I., et al. 2020, ApJ, 889, 93
- van der Wel, A., van Houdt, J., Bezanson, R., et al. 2022, ApJ, 936, 9
- Veilleux, S., Cecil, G., & Bland-Hawthorn, J. 2005, ARA&A, 43, 769
- Veilleux, S., Maiolino, R., Bolatto, A. D., & Aalto, S. 2020, A&A Rev., 28, 2
- Wang, T., Xu, K., Wu, Y., et al. 2024, Nature, 632, 1009
- Weibel, A., de Graaff, A., Setton, D. J., et al. 2025, ApJ, 983, 11
- Weibel, A., Oesch, P. A., Barrufet, L., et al. 2024, MNRAS, 533, 1808
- Weiner, B. J., Coil, A. L., Prochaska, J. X., et al. 2009, ApJ, 692, 187
- Witstok, J., Jones, G. C., Maiolino, R., Smit, R., & Schneider, R. 2023, MNRAS, 523, 3119
- Worthey, G. & Ottaviani, D. L. 1997, ApJS, 111, 377
- Wu, P.-F. 2025, ApJ, 978, 131
- Xie, L., De Lucia, G., Fontanot, F., et al. 2024, ApJ, 966, L2
- Xu, X., Heckman, T., Henry, A., et al. 2022, ApJ, 933, 222
- <sup>22</sup> Department of Astronomical Science, The Graduate University for Advanced Studies, SOKENDAI, 2-21-1 Osawa, Mitaka, Tokyo 181-8588, Japan
- <sup>23</sup> National Astronomical Observatory of Japan, 2-21-1 Osawa, Mitaka, Tokyo 181-8588, Japan
- <sup>24</sup> School of Science, Kwansei Gakuin University, 2-1, Gakuen, Sanda, Hyogo 669-1337, Japan
- <sup>25</sup> Astronomical Institute, Tohoku University, Aoba-ku, Sendai 980-8578, Japan
- <sup>26</sup> International Centre for Radio Astronomy Research (ICRAR), M468, University of Western Australia, 35 Stirling Hwy, Crawley, WA 6009, Australia
- <sup>27</sup> Department of Physics & Astronomy, University of British Columbia, 6224 Agricultural Road, Vancouver BC, V6T 1Z1, Canada
- <sup>28</sup> Subaru Telescope, National Astronomical Observatory of Japan, National Institutes of Natural Sciences (NINS), 650 North A'ohoku Place, Hilo, HI 96720, USA
- <sup>29</sup> Kapteyn Astronomical Institute, University of Groningen, Landleven 12, 9747 AD, Groningen, The Netherlands
- <sup>30</sup> Waseda Institute for Advanced Study (WIAS), Waseda University, 1-21-1 Nishi-Waseda, Shinjuku, Tokyo 169-0051, Japan
- <sup>31</sup> Center for Interdisciplinary Exploration and Research in Astrophysics (CIERA), Northwestern University, 1800 Sherman Ave, Evanston, IL 60201, USA
- <sup>32</sup> Graduate Institute of Astrophysics, National Taiwan University, Taipei 10617, Taiwan

- <sup>1</sup> Cosmic Dawn Center (DAWN), Denmark
- <sup>2</sup> DTU Space, Technical University of Denmark, Elektrovej 327, DK-2800 Kgs. Lyngby, Denmark
- <sup>3</sup> European Southern Observatory, Karl-Schwarzschild-Str. 2, 85748 Garching, Germany
- <sup>4</sup> Niels Bohr Institute, University of Copenhagen, Jagtvej 128, 2200, Copenhagen N, Denmark
- <sup>5</sup> Department of Astronomy, University of Geneva, Chemin Pegasi 51, 1290 Versoix, Switzerland
- <sup>6</sup> Department of Astronomy, School of Science, The University of Tokyo, 7-3-1, Hongo, Bunkyo-ku, Tokyo, 113-0033, Japan
- <sup>7</sup> Department of Astronomy, The University of Texas at Austin, Austin, TX 78712, USA
- <sup>8</sup> Department of Astronomy, University of Massachusetts, Amherst, MA 01003, USA
- <sup>9</sup> INAF - Osservatorio Astrofisico di Arcetri, Largo Enrico Fermi 5, 50125 Firenze, Italy
- <sup>10</sup> Max-Planck-Institut für Astronomie, Königstuhl 17, D-69117, Heidelberg, Germany
- <sup>11</sup> Department of Astronomy/Steward Observatory, University of Arizona, 933 N Cherry Ave., Tucson, AZ 85721-0009, USA
- <sup>12</sup> School of Earth and Space Exploration, Arizona State University, PO Box 876004, Tempe, AZ 85287-6004, USA
- <sup>13</sup> Departamento de Física Teórica, Modulo 8, Facultad de Ciencias, Universidad Autónoma de Madrid, 28049 Madrid, Spain
- <sup>14</sup> CIAFF, Facultad de Ciencias, Universidad Autónoma de Madrid, 28049 Madrid, Spain
- <sup>15</sup> Caltech/IPAC, MS 314-6, 1200 E. California Blvd. Pasadena, CA 91125, USA
- <sup>16</sup> Institute of Physics, Laboratory for Galaxy Evolution, EPFL, Observatoire de Sauverny, Chemin Pegasi 51, 1290 Versoix, Switzerland
- <sup>17</sup> Joint ALMA Observatory, Alonso de Córdova 3107, Vitacura, Casilla 19001, Santiago de Chile, Chile
- <sup>18</sup> National Astronomical Observatory of Japan, Los Abedules 3085 Oficina 701, Vitacura 763 0414, Santiago, Chile
- <sup>19</sup> European Southern Observatory, Alonso de Córdova 3107, Vitacura, Casilla 19001, Santiago de Chile, Chile
- <sup>20</sup> Universidad Diego Portales, Av. Ejercito Santiago de Chile, Chile
- <sup>21</sup> Department of Astrophysical Sciences, Princeton University, Princeton, NJ 08544, USA



## Appendix A: Extended spectra of NS\_274

For full transparency, we ran the customized MSAEXP pipeline also on the G140M and G235M spectra of NS\_274. In this case, the advantage of extending the G140M spectrum is marginal compared with the gain obtained by processing the bluest spectrum of RUBIES-UDS-QG-z7 – simply because a deep coverage of the rest-frame optical wavelengths is already available. The G235M grating spectrum extension covers the  $H\alpha$  Balmer line and the  $[\text{N II}]\lambda\lambda 6549, 6585$  doublet. However, in the case of NS\_274, the extension comes with an uncertain absolute flux calibration and a systematic color gradient compared with the PRISM spectrum. For reference, we reran the same pPXF modeling described in Sect. 3.1 and estimate a stellar velocity dispersion of  $\sigma_\star = 278 \pm 23$   $\text{km s}^{-1}$ , 10% higher than, but in agreement with the value in Table 1. We also estimate observed (thus, magnified) line fluxes of  $[\text{Ne III}] = 2.8^{+2.6}_{-2.4}$ ,  $[\text{O II}] = 4.0^{+3.0}_{-2.8}$ ,  $H\beta = 2.3^{+2.2}_{-2.3}$ ,  $[\text{O III}] = 8.9^{+2.6}_{-2.8}$ ,  $H\alpha = 15.4^{+3.2}_{-3.5}$ , and  $[\text{N II}]\lambda 6585 = 37.5^{+5.0}_{-4.9}$  all expressed in units of  $10^{-19} \text{ erg cm}^{-2} \text{ s}^{-1}$ . We stress that the flux calibration uncertainties, and especially the color term, influence the line fluxes and their ratios non trivially, as the stellar continuum absorption features have to be modeled in order to derive the line emission. This explains the difference in the  $H\beta$  flux measurement and its ratio with  $[\text{O III}]$  ( $\log([\text{O III}]/H\beta) > -0.37$  ratio at  $3\sigma$  in the extended spectrum). At face value, we estimate  $\log([\text{N II}]/H\alpha) = 0.39^{+0.13}_{-0.11}$  (where the uncertainties are purely statistical), which would place NS\_274 beyond the extrapolation to  $z = 4$  of the line dividing star-forming galaxies and AGNs in the BPT diagram (Baldwin et al. 1981) presented in Kewley et al. (2013). We note that the parameterization in Kewley et al. (2013) is not calibrated against data at  $z = 4$  and should be taken with a grain of salt. If confirmed, these emission line ratios would be potential evidence of a faint AGN-powered emission, or at least non-star-formation-powered ionized emission, as first proposed in Wu (2025). Future, deeper observations will test this possibility.

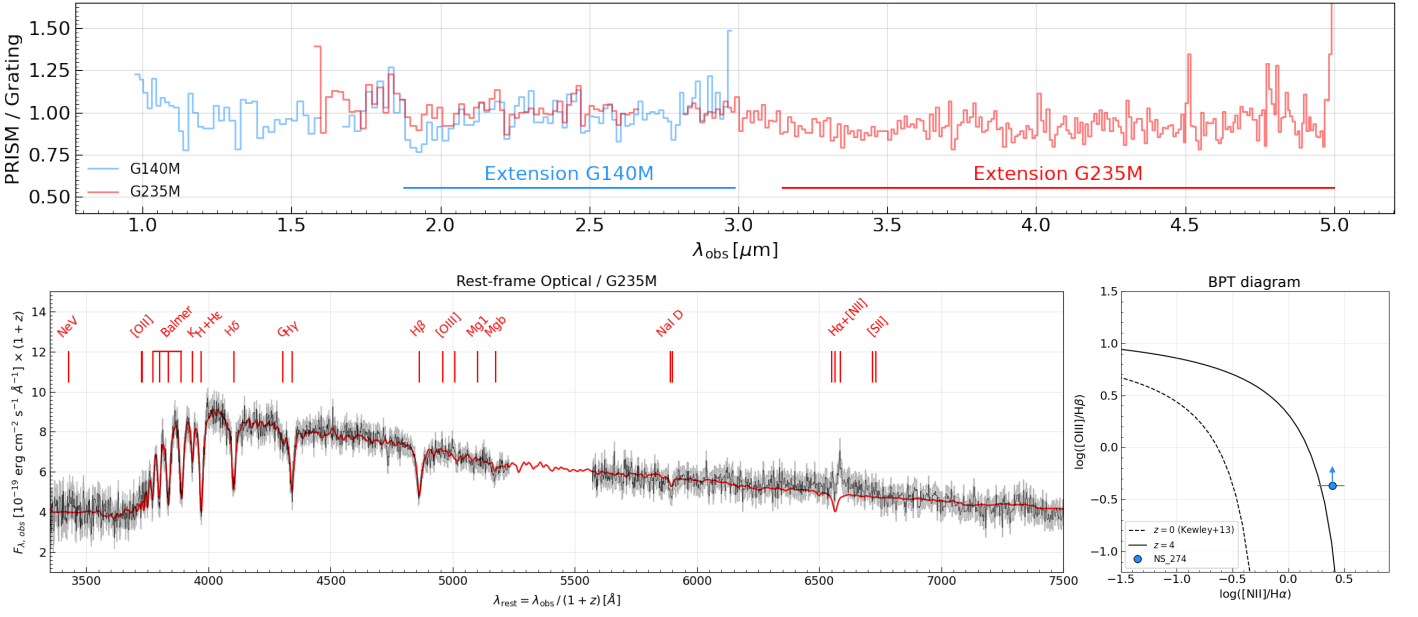


Fig. A.1: Top: Flux density ratio between the PRISM and the G140M (blue line) and G235M (red line) grating spectra in the custom reduction of NS\_274. We mark with a solid line the extended wavelength coverage. Bottom: Extended G235M spectrum of NS\_274 (black) and its uncertainties (gray). The red line indicates the best-fit pPXF model of the stellar continuum. The panel on the right shows the location of the source in the BPT diagram based on the measurements in the extended G235M spectrum. The dashed and solid black lines indicate the empirical parameterization of the line dividing star-forming galaxies and AGNs by Kewley et al. (2013) at  $z = 0$  and  $z = 4$ , respectively.

## Appendix B: Modeling supplementary material

In Fig. B.1 we show the posterior distributions of the parameters obtained by modeling the spectra and photometry of NS\_274 and RUBIES-UDS-QG-z7 as detailed in Sect. 3.1. Properties of the priors are reported in Table B.1. We show them in Fig. B.2. In Fig. B.3 we report the results of the joint best-fit modeling of the G235M and G395M spectra of RUBIES-UDS-QG-z7 to determine its exact spectroscopic redshift (see Sect. 2.2). Finally, Fig. B.4 shows the NIRCам/F200W image of NS\_274, the best-fit Sérsic described in Sect. 3.3, and the residuals.

Table B.1: Free parameters and priors for the spectrophotometric modeling.

Free parameter	Prior	Limits
$\log(M_{\text{formed}}/M_\odot)$	Uniform	(9, 11.5)
$A_V$	Uniform	(0, 2)
$Z/Z_\odot$	Uniform	(0.1, 2)
$\tau/\text{Gyr}$	Uniform	(0, $t(z_{\text{obs}})$ )
$\alpha, \beta$	Logarithmic	( $10^{-2}$ , $10^{-3}$ )
Noise rescale $s_{\text{noise}}$	Logarithmic	(1, 10)

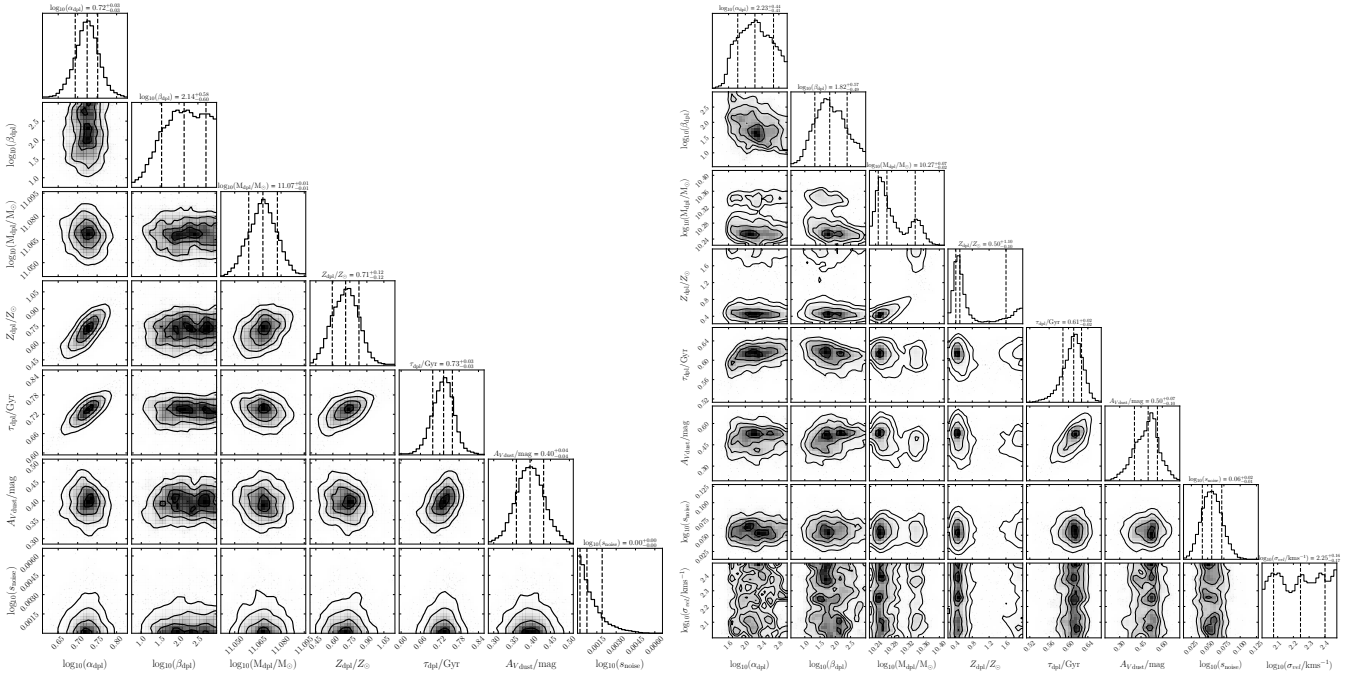


Fig. B.1: Corner plots showing the posterior distributions of the parameters constrained with BAGPIPES as detailed in Sect. 3.1. Left: NS\_274 at  $z = 4.1061$ ; Right: RUBIES-UDS-QG-z7 at  $z = 7.2758$ .

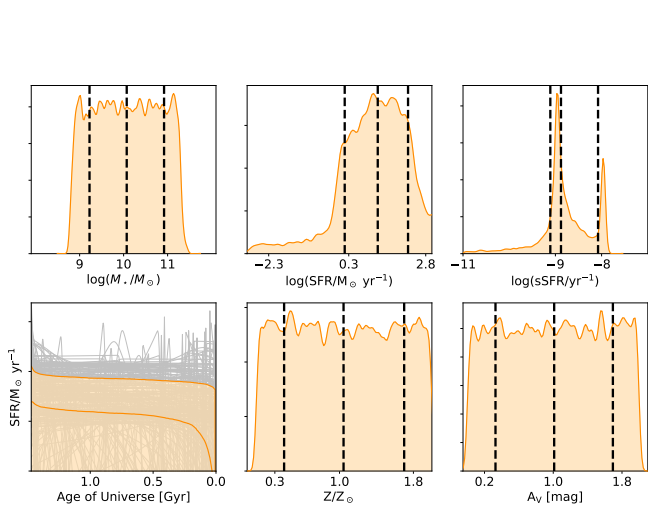


Fig. B.2: Priors on the parameters listed in Table B.1 for NS\_274. Dashed black lines indicate the 16, 50, and 84% percentiles of the distributions. In the SFH panel, we show randomly extracted SFHs in gray. The orange area shows the 16-84% inter-percentile range. Similar priors were applied to model the spectrum and photometry of RUBIES-UDS-QG-z7.

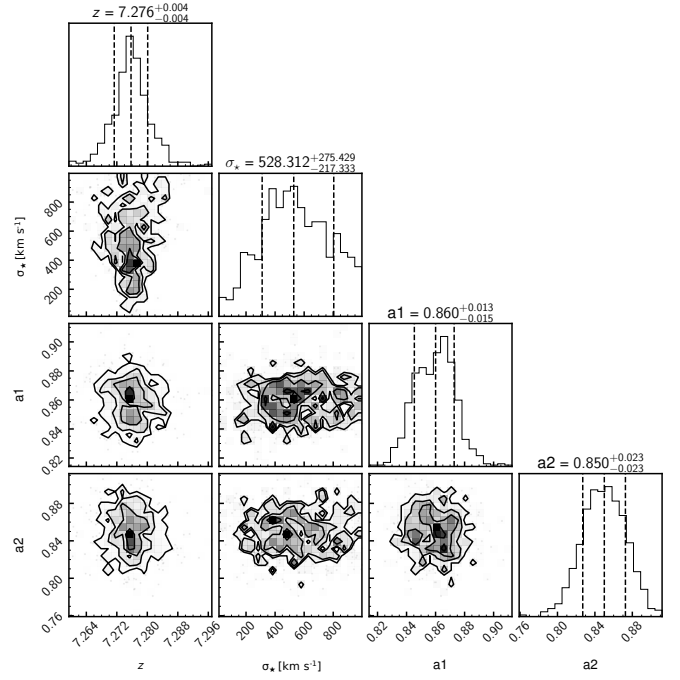


Fig. B.3: Corner plot showing the posterior distributions of the free parameters of the template scaling used to determine the redshift of RUBIES-UDS-QG-z7.

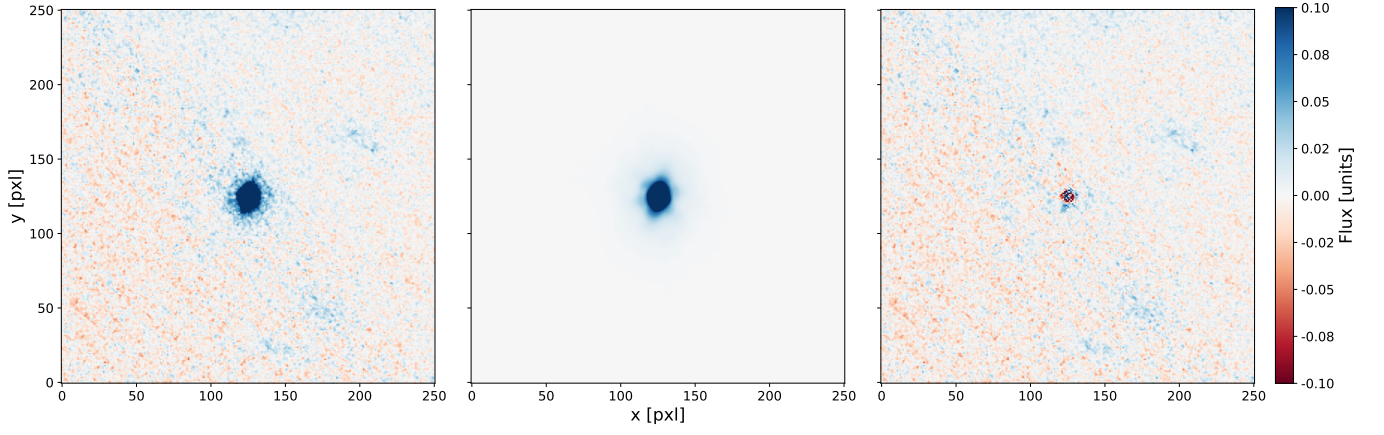


Fig. B.4: Sérsic modeling of NS\_274. *Left:*  $5'' \times 5''$  ( $\sim 35 \times 35$  kpc at  $z = 4.1$ ) F200W cutout image of our target. *Center:* Best-fit Sérsic model (Sect. 3.3). *Right:* Residuals computed by subtracting the best-fit model from the input image.